Skin tumor delineation using photoacoustic imaging and hyperspectral imaging

Hult, Jenny

2024

Document Version:
Publisher's PDF, also known as Version of record

Skin tumor delineation using photoacoustic imaging and hyperspectral imaging

JENNY HULT
OPHTHALMOLOGY | FACULTY OF MEDICINE | LUND UNIVERSITY

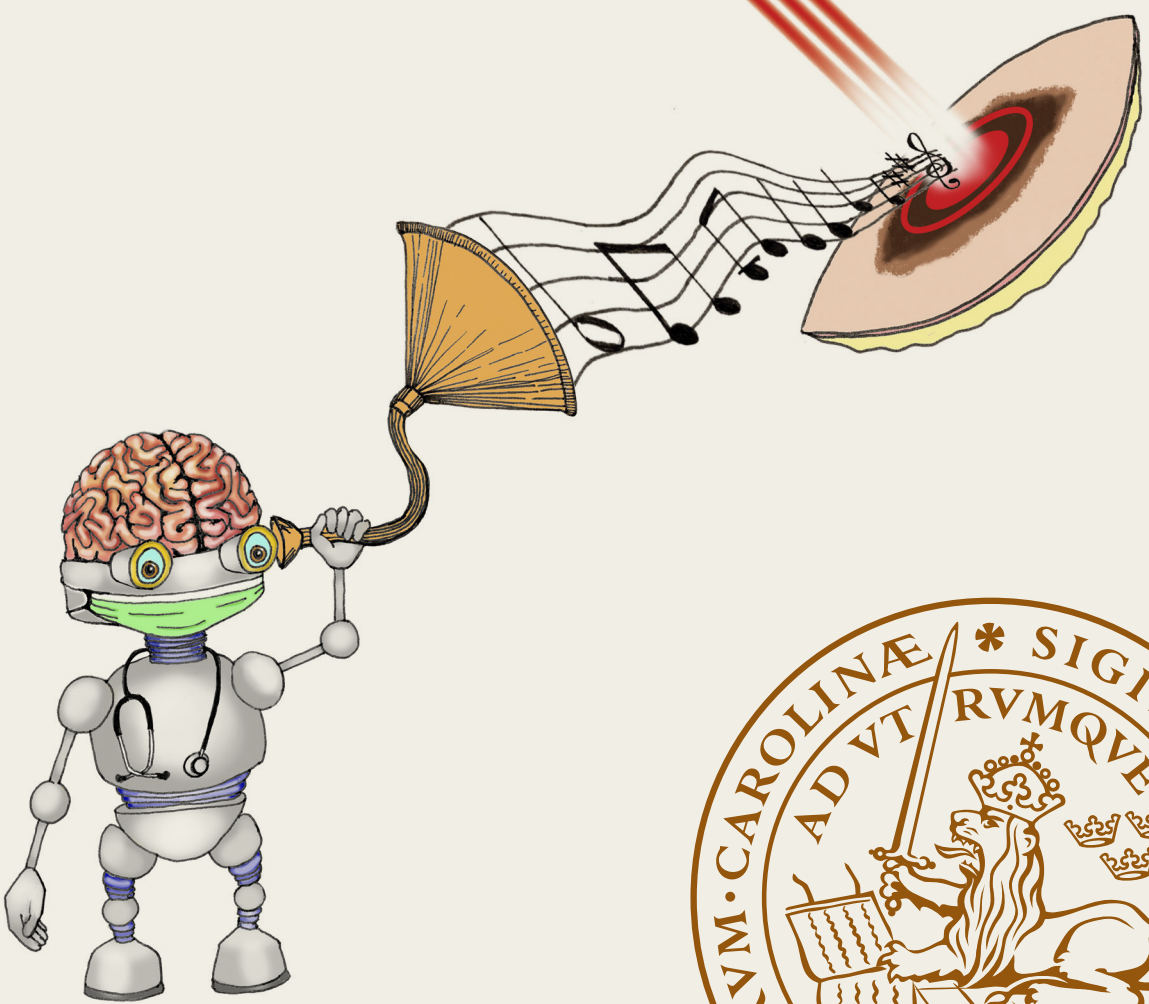

Printed by Media-Tryck, Lund 2024 NORDIC SWAN ECOLABEL 3041 0903

Skin tumor delineation using photoacoustic imaging and hyperspectral imaging

Skin tumors suspected of malignancy are usually treated with surgical excision. To increase the probability of removing all the tumor cells while protecting healthy tissue, there is a need for an imaging technique that can guide surgery. In this dissertation, two novel techniques (photoacoustic imaging and hyperspectral imaging) were explored for non-invasive imaging and delineation of skin tumors.

LUND UNIVERSITY

FACULTY OF MEDICINE

Department of Clinical Sciences Lund
Ophthalmology

Lund University, Faculty of Medicine
Doctoral Dissertation Series 2024:133
ISBN 978-91-8021-631-9
ISSN 1652-8220

Skin tumor delineation using photoacoustic imaging and hyperspectral imaging

Jenny Hult, MD

LUND
UNIVERSITY

DOCTORAL DISSERTATION

by due permission of the Faculty of Medicine, Lund University, Sweden.
To be defended at 1:00 PM on November 22nd 2024, in
LUX aula, Helgonavägen 3, Lund, Sweden

Faculty opponent
Mette Mogensen, MD, PhD

Associate Professor, University of Copenhagen, Denmark

Organization LUND UNIVERSITY Faculty of Medicine Department of Clinical Sciences Lund, Ophthalmology, Lund Sweden	**Document name** DOCTORAL DISSERTATION
	Date of issue 2024-11-22
Author: Jenny Hult	Sponsoring organization

Title and subtitle

Skin tumor delineation using photoacoustic imaging and hyperspectral imaging

Abstract

To decrease the risk of non-radical excisions of skin tumors while preserving healthy tissue, there is a need for an imaging technique that can guide surgery. Several non-invasive imaging techniques have been studied for this purpose, but most techniques suffer from limitations such as shallow imaging depths or an inability to image molecular contents. Spectral techniques including hyperspectral imaging (HSI) and photoacoustic imaging (PAI) can provide molecular contrast and have the potential to differentiate between tumor tissue and healthy tissue, which can be used for tumor imaging and delineation of tumor borders. While HSI collects spectral information from the skin surface, PAI combines laser light and ultrasound to collect spectral information from deeper parts of the skin than was previously possible with other optical techniques. Hence, the techniques enable 2D and 3D imaging. Only a few small studies have explored HSI and PAI for the purpose of skin tumor delineation, and all used different settings and methods for spectral analysis. The aim of this dissertation was to explore and develop spectral techniques for imaging and delineation of skin tumors. By developing algorithms and machine learning methods, we attempted to make the imaging analysis more objective and independent of the user.

In the first study, suspected cutaneous squamous cell carcinomas (cSCCs) were imaged *ex vivo* using PAI. The results showed a unique spectral absorption signal for confirmed cSCCs and demonstrated how the signal could be used for 3D tumor imaging. In the second study, suspected malignant melanomas were scanned *ex vivo* using PAI. An automatic threshold algorithm for identifying and delineating the tumors was developed. The PAI measured tumor widths and thicknesses were compared to histopathological measurements, showing strong correlations for the melanomas. In the third study, a statistical detection method called adaptive matched filter (AMF) was explored using an automatic threshold selection (ATS) algorithm for imaging of *ex vivo* melanomas. The study showed a superior performance for the ATS algorithm compared to fixed threshold values, and a good correlation to histopathological thickness measurements. In the fourth study, machine learning in the form of 3 different neural networks was used on HSI data from various tumors imaged *ex vivo*. Using spectral signals from tumor and healthy skin as training, it was demonstrated that the networks could make 2D tumor predictions at the skin surface. A segmentation algorithm was used to delineate the tumors and the tumor widths could then be compared to histopathological measurements. The results showed that 4 of the tumors could not be delineated due to noise. For the remaining 14 tumors, the width correlations were strong for all 3 networks.

In conclusion, the papers in this dissertation demonstrate the feasibility for spectral imaging and delineation of skin tumors, which is important for more precise surgical excisions in the future.

Key words Skin cancer, photoacoustic imaging, hyperspectral imaging, adaptive matched filter, machine learning

Classification system and/or index terms (if any)

Supplementary bibliographical information		**Language** English
ISSN and key title: 1652-8220		**ISBN** 978-91-8021-631-9
Recipient's notes	**Number of pages** 82	Price
	Security classification	

Skin tumor delineation using photoacoustic imaging and hyperspectral imaging

Jenny Hult, MD

LUND
UNIVERSITY

Cover illustration by Jenny Hult

Lund University, Faculty of Medicine Doctoral Dissertation Series 2024:133
ISBN 978-91-8021-631-9
ISSN 1652-8220

Printed in Sweden by Media-Tryck, Lund University, Lund 2024

Til Theis, Enna,
Björk og Karl-Erik

‘I have heard articulate speech by sunlight! I have heard a ray of the sun laugh and cough and sing! …… I have been able to hear a shadow and I have even perceived by ear the passage of a cloud across the sun’s disk.’

Alexander Graham Bell

Abstract

Skin cancer is one of the most common types of cancer worldwide. Malignant skin tumors that are not completely removed by surgical excision or other kinds of treatment will grow locally and cause tissue destruction, and some will metastasize to lymph nodes or other organs. In some tumors, the superficial borders are ill-defined, and for all tumors, the extent of the tumor beneath the surface is usually invisible to the naked eye or the commonly used dermatoscope. To increase the probability of removing all the tumor cells during surgery, while preserving healthy tissue, there is a need for an imaging technique that can guide surgery. Several non-invasive imaging techniques have been studied for this purpose, but most of them suffer from limitations, such as shallow imaging depth or an inability to image the molecular content. Spectral techniques, including hyperspectral imaging and photoacoustic imaging, can provide molecular contrast and have the potential to differentiate between tumor tissue and healthy tissue. While hyperspectral imaging collects spectral information from the skin surface, photoacoustic imaging uses light-induced ultrasound signals to obtain spectral information from deeper layers of the skin than has been possible with other optical techniques. Only a few small studies have explored hyperspectral imaging and photoacoustic imaging for the purpose of skin tumor delineation, and different settings and methods were used for spectral analysis. The aim of the work presented in this dissertation was to explore and develop spectral techniques for imaging and delineation of skin tumors. The skin tumors were examined *ex vivo*, and differences in the spectral contrast between the tumor and the surrounding healthy tissue was used to image and delineate the tumors. Through the development of algorithms and machine learning methods, attempts were made to make the imaging analysis more objective and independent of the user. The results of the studies demonstrated the potential of these new spectral techniques for 2D and 3D delineation of skin tumors. The development of non-invasive imaging techniques for skin tumor delineation is important to ensure complete and precise surgical excision, thus reducing the risk of non-radicality or excessive removal of healthy tissue. Further developments and *in vivo* studies are, however, required to make the techniques suitable for future clinical use.

Overview of publications

Below follows a brief introduction to the papers included in this dissertation. The papers will be referred to in the text by their Roman numerals and are appended at the end of the dissertation.

Paper I

Unique spectral signature of human cutaneous squamous cell carcinoma by photoacoustic imaging.

Hult J, Dahlstrand U, Merdasa A, Wickerström K, Chakari R, Persson B, Cinthio M, Erlöv T, Albinsson J, Gesslein B, Sheikh R, Malmsjö M.

J Biophotonics. 2020 May;13(5):e201960212

Cutaneous squamous cell carcinoma (cSCC) is a common skin cancer with metastatic potential. Suspected tumors are usually removed surgically with internationally recommended macroscopic margins, followed by histopathological examination to confirm that the margins are clear of tumor cells. If the margins are not clear, the patient must undergo further surgery until the tumor is completely removed. Photoacoustic imaging (PAI) can provide unique, spectral signatures of different kinds of tissue, depending on their molecular composition, and high resolution at a depth of several mm in skin. It has the potential to differentiate between healthy and diseased tissue and to image the whole extent of a skin tumor in 3D.

The aim of this study was to investigate whether it was possible to identify a unique spectral signature for human cSCCs, and to determine whether the mean spectral signature could be used to visualize the tumor architecture and borders.

Paper II

Comparison of photoacoustic imaging and histopathological examination in determining the dimensions of 52 human melanomas and nevi ex vivo.

Hult J, Merdasa A, Pekar-Lukacs A, Tordengren Stridh M, Khodaverdi A, Albinsson J, Gesslein B, Dahlstrand U, Engqvist L, Hamid Y, Larsson Albèr D, Persson B, Erlöv T, Sheikh R, Cinthio M, Malmsjö M.

Biomed Opt Express. 2021 Jun 15;12(7):4097-4114.

Malignant melanoma is the most lethal type of skin cancer. Swedish guidelines recommend that suspected melanomas should be excised with a 2 mm visible margin, and if the diagnosis is confirmed a wide local excision is performed, with 1 or 2 cm margins depending on the tumor thickness. As with cSCCs, a technique capable of determining the melanoma borders and dimensions could guide the first diagnostic excision and reduce the need for reoperation or unnecessary removal of healthy tissue.

The aim of the study presented in Paper II, was to image melanomas in 3D with PAI. In this study, individual tumor spectra were used for imaging of the tumors instead of mean tumor spectra, as in the first study. A threshold algorithm was developed for tumor pixel identification and delineation, and the tumor width and thickness were compared to histopathological measurements.

Paper III

Automatic threshold selection algorithm to distinguish a tissue chromophore from the background in photoacoustic imaging.

Khodaverdi A, Erlöv T, **Hult J**, Reistad N, Pekar-Lukacs A, Albinsson J, Merdasa A, Sheikh R, Malmsjö M, Cinthio M.

Biomed Opt Express. 2021 Jun 4;12(7):3836-3850.

In the previously papers, a common spectral analysis method, linear spectral unmixing, was used to image the tumors. Linear spectral unmixing attempts to resolve all the spectral components in an image. In contrast, the adaptive matched filter (AMF) method is a statistical method that focuses solely on the detection of a distinct spectral target (e.g. a tumor spectrum) and suppresses signals from the background (e.g. healthy tissue). An advantage of AMF, compared to linear spectral unmixing, is that AMF can reduce the undesirable effects of spectral

coloring, which is a wavelength-dependent change in the spectral response of different absorbers. When applied to PA data, AMF produces a so-called 'detection image' in which the amplitude corresponds to the target (tumor spectrum) probability. Therefore, to obtain a sharp distinction between the target and background pixels, a threshold must be applied.

The aim of the study described in Paper III was to explore the use of AMF in PAI, and to develop an automatic threshold selection (ATS) algorithm that could be applied to AMF detection images. The ATS algorithm was developed using a tissue-mimicking phantom and tested on 7 melanomas *ex vivo*. The results were compared to histopathological measurements.

Paper IV

Facilitating clinically relevant skin tumor diagnostics with spectroscopy-driven machine learning.

Andersson E, **Hult J**, Troein C, Stridh M, Sjögren B, Pekar-Lukacs A, Hernandez-Palacios J, Edén P, Persson B, Olariu V, Malmsjö M, Merdasa A.

iScience. 2024 Apr 1;27(5):109653.

Hyperspectral imaging (HSI) is a non-invasive imaging technique that can detect how tissue responds to light using a large number of wavelengths both within and beyond the visible spectrum. The technique has a very high spectral and spatial resolution at the skin surface, where it enables detailed imaging. Since the amount of data generated is vast, processing and analysis of the data are difficult with conventional methods, but can be facilitated by the use of machine learning.

A growing number of studies have implemented machine learning to facilitate the diagnosis and delineation of skin tumors. Machine learning trains on a dataset to improve a computer algorithm. The algorithm can then make predictions about new, raw data. A problem with previous studies on machine learning for skin tumor delineation is that the models have been trained on manually delineated skin tumors, which is subjective and prone to errors unless the borders are precisely matched with histopathological borders.

The aim of the study presented in Paper IV was to delineate skin tumors on the skin surface using HSI and machine learning. The machine learning models were trained on hyperspectral data obtained from regions with and without tumors lesions suspected of being basal skin carcinoma (BCC), cSCC or melanoma, without any manual input of the tumor borders. The trained models then made predictions of the tumor probability in each pixel. Pixels with high tumor

probability were classified as tumor. Algorithms were then used to track the outlines of the predicted tumors. Finally, the performance of the models was evaluated by correlating the model-predicted tumor widths to widths determined histopathologically.

Dissertation at a glance

PAPER	AIM	TUMOR TYPES	NUMBER OF TUMORS	TECHNIQUE	METHOD OF PIXEL CLASSIFICATION
I	To identify a unique spectral signature for cSCCs *ex vivo*, and to use the signal for tumor imaging	cSCCs	33	Photoacoustic imaging	Linear spectral unmixing
II	To image and delineate melanomas *ex vivo* in 3D using individual tumor spectra	Nevi and melanomas	52	Photoacoustic imaging	Linear spectral unmixing
III	To explore a statistical detection method (AMF) and develop an automatic threshold selection algorithm for 3D delineation of melanomas *ex vivo*	Melanomas	7	Photoacoustic imaging	Adaptive matched filter
IV	To image and delineate skin tumors at the skin surface in 2D *ex vivo*	BCCs cSCCs Nevi Melanomas	18	Hyperspectral imaging	Machine learning

Preface

In my childhood home, we had a small library filled with medical books and atlases. I used to spend hours looking through these books, fascinated by the range of diseases that could affect the human body. Later, in medical school in Copenhagen, I learned that many diseases of the eye could readily be diagnosed with the aid of new imaging systems. This caught my attention and led me to write my master's thesis on keratoconus, a corneal disease which, due to the transparency of the cornea, can be imaged in detail in 3D, and diagnosed at an early stage with optical techniques available at the clinic.

As a clinician, one wishes that all diseases could be diagnosed as quickly and accurately as keratoconus. Malignant tumors of the eyelid and skin are common, but their diagnosis cannot be established without a biopsy or excision. Furthermore, the excision of a suspected malignant tumor poses a problem as the extent of the tumor is often not visible to the naked eye, and clinically available imaging techniques have limitations that often make them unsuitable for this purpose. The studies presented in this dissertation explore new spectral techniques for skin tumor imaging, with the hope of eventually being able to delineate tumors accurately *in vivo* to guide surgical removal. Although the tumors were imaged *ex vivo*, in these studies, the clinical perspective was central; imaging of skin tumors should be carried out with non-ionizing radiation and cause as little discomfort to the patient as possible. Furthermore, delineation of the tumors should be a quick and objective process, independent of the experience of the clinician or surgeon.

During my PhD studies, I learnt that achieving the objective of precise tumor delineation was not trivial, which was initially frustrating. I gradually started to regard my research from a broader perspective, and understood that all results, even small, are important in the ongoing, international process of understanding, developing, and using such techniques. I hope that the work presented in this dissertation will provide insights into the potential of the techniques studied, and ways in which they can be used, for skin tumor imaging or other medical purposes, and contribute to further research.

Populärvetenskaplig sammanfattning

Hudcancer är en av de vanligaste cancerformerna i världen. En misstänkt elakartad hudtumör opereras idag oftast bort med en förutbestämd marginal, då man med dagens tillgängliga undersökningsmetoder inte kan avgöra tumörens utbredning med säkerhet, varken ytligt eller på djupet. Efter operationen skickas tumören till patolog för histopatologisk undersökning, där patologen genom infärgningar och mikroskopi avgör om tumören är bortopererad i sin helhet. Om patologen misstänker att det kan finnas tumörceller kvar i huden måste patienten som regel opereras igen. Risken för att en andra operation behöver genomföras måste vägas mot risken med att operera med stora marginaler omkring tumören, vilket kan ge patienten missprydande ärr och funktionella problem i området. Ett alternativ är Mohs kirurgi, där vävnad mikroskoperas i samband med operationen för att säkra att det inte finns tumörceller kvar i huden. Mohs kirurgi är dock tidskrävande och kräver specialutbildad personal samt tillgång till ett histopatologiskt laboratorium med avancerad utrustning.

Den svåra balansen mellan att riskera att ta bort för mycket eller för lite hud omkring tumören skulle kunna undvikas om tumörens utbredning kunde avgöras innan operationen, eller under operationen precis som vid Mohs kirurgi. Problematiken är välkänd, och flera studier har gjorts för att hitta en teknik som kan identifiera tumörernas exakta utbredning. De flesta tekniker är rent ljusbaserade och har fördelen av hög upplösning i hudens yttersta lager. Dessa tekniker kan som regel bidra med strukturell information om tumörerna, men saknar oftast förmågan att åtskilja signaler från olika molekyler, till exempel melanin, hemoglobin och fett. Spektrala avbildningstekniker har fördelen att de använder flera olika våglängder av ljus för att analysera vävnad, vilket kan ge information om vävnadens molekylära sammansättning samt hitta skillnader mellan signaler från frisk och sjuk vävnad.

Syftet med denna avhandling var att undersöka om nya spektrala avbildningstekniker kunde avbilda och avgränsa hudtumörer både ytligt och på djupet. De tekniker som användes för undersökning var fotoakustik och hyperspektral avbildning. Fotoakustik är en teknik som baseras på en upptäckt av Dr. Alexander Graham Bell från år 1880. Dr. Bell visade att tunna skivor av olika material avgav ljud när de kortvarigt värmdes upp av ryckvis återkommande solljusstrålar, ett fenomen som han kallade för den ”fotoakustiska effekten”. Fotoakustik skiljer sig från andra optiska tekniker genom att de ljussignaler som

skickas in i vävnad omvandlas till ljud. Eftersom ljud har en mindre spridning i vävnad än ljus har fotoakustik potential att avbilda vävnad på flera millimeters djup samtidigt som tekniken behåller en god upplösning, vilket inte tidigare har varit möjligt med optiska tekniker. Fotoakustik har därmed förmåga att avbilda hudtumörer i 3D. Hyperspektral avbildning är en annan spektral avbildningsteknik som kan användas för att analysera hudens yta. Vitt ljus används för att belysa vävnad, och den reflekterade signalen delas upp i flera hundra våglängder vilket gör att tekniken kan hitta små skillnader i den molekylära signalen mellan frisk och sjuk vävnad.

I denna avhandling undersöktes hudtumörer som precis hade opererats bort.

I den första studien utforskades fotoakustikens potential för avbildning av skivepitelcancer, en av de vanligaste, elakartade hudcancerformerna. Resultatet visade att skivepitelcancer har en spektral signal som skiljer sig signifikant från frisk hud och att signalen kan användas till avbildning.

I den andra studien undersöktes misstänkta maligna melanom, som är den dödligaste hudcancerformen, med hjälp av fotoakustik. I studien användes varje tumörs individuella tumörsignal som utgångspunkt för avbildning, och en automatisk algoritm användes för att åtskilja tumör från frisk vävnad. Genom att jämföra tumörernas fotoakustiska mått med histopatologiska mått kunde ett starkt samband påvisas gällande melanomens bredd och tjocklek.

I den tredje studien analyserades fotoakustisk data från bekräftade maligna melanom med hjälp av en statistisk modell som heter AMF (*adaptive matched filter*). Genom att utveckla en automatisk algoritm kunde ett tröskelvärde bestämmas för att urskilja misstänkta tumörpixlar. Resultaten tydde på ett bra samband mellan fotoakustiska mått och histopatologiska mått av tumörernas tjocklek.

I den fjärde studien togs ytterligare ett steg bortom mänsklig inblandning i dataanalys. I denna studie undersöktes flera olika hudtumörer med hjälp av hyperspektral avbildning. Därefter användes *machine learning*, ett område inom artificiell intelligens, för att urskilja hudtumörer från omkringliggande frisk hud. I tidigare studier som använt machine learning på spektroskopisk data från hudtumörer har man oftast ‘tränat’ nätverken genom att rita ut tumörgränser manuellt. Detta heter att man skapar *ground truth images*, men har nackdelen av att gränserna ju inte kan definieras med säkerhet med blotta ögat. I denna studien tränades nätverken på pixlar i centrum av tumören samt på pixlar i frisk vävnad utanför tumören för att avbilda och avgränsa tumören, vilket gjorde att man kunde undvika att markera ut tumörgränser manuellt . Resultatet visade att några av tumörerna inte kunde avbildas pga. brus, men i resterande tumörer kunde bredden mätas och jämföras med histopatologiska mått. Jämförelsen visade ett starkt samband.

Samlat sett pekar studierna i denna avhandling på att spektral avbildning har potential att kunna användas för avgränsning av hudtumörer, vilket skulle kunna möjliggöra mer precis kirurgi i framtiden. Mer forskning med ett bredare patientunderlag behövs dock innan teknikerna kan användas kliniskt.

Contents

Abstract ..... **vii**

Overview of publications ..... **viii**

Paper I viii

Paper II ix

Paper III ix

Paper IV x

Dissertation at a glance xi

Preface ..... **xii**

Populärvetenskaplig sammanfattning ..... **xiii**

Contents ..... **xvi**

Abbreviations ..... **xviii**

Introduction **1**

Skin anatomy 2

Skin tumors and their treatment 3

Basal cell carcinoma 4

Cutaneous squamous cell carcinoma 5

Malignant melanoma 5

Histopathologic examination 6

Mohs micrographic surgery 6

Non-invasive techniques for skin tumor imaging 7

Dermatoscopy 7

Optical coherence tomography 8

Reflectance confocal microscopy 8

High-frequency ultrasound 9

Other techniques 9

Spectral imaging 10

Photoacoustic imaging 12

Hyperspectral imaging 17

Spectral analysis 18
Linear spectral unmixing 18
Adaptive matched filter 19
Machine learning 19

Aims 22

Specific aims 22

Materials and methods 23

Ethics 23

Subjects and tumors 24

Safety aspects 24

Experimental setup and equipment 25
Experimental setup 25
Photoacoustic imaging equipment 27
Hyperspectral imaging equipment 27

Imaging of skin tumors 29
Photoacoustic imaging of cSCCs using linear spectral unmixing 29
Photoacoustic imaging of melanomas and nevi using linear spectral unmixing 29
Photoacoustic imaging of melanomas using AMF 30
Hyperspectral imaging of various skin tumors using machine learning 31

Statistical analysis 32
Comparison of tumor and healthy spectra 32
Comparison of imaging measurements with histopathological measurements 33

Results and discussion 34

Photoacoustic imaging of cSCCs 34

Photoacoustic imaging of melanomas and nevi 36

Hyperspectral imaging and machine learning for delineation of superficial tumor borders 41

Skin types 46

Differential diagnosis 46

Conclusions and future perspectives 47

Acknowledgements 48

References 51

Abbreviations

AMF	Adaptive matched filter
ANN	Artificial neural network
ATS	Automatic threshold selection
BCC	Basal cell carcinoma
cSCC	Cutaneous squamous cell carcinoma
CNN	Convolutional neural network
HSI	Hyperspectral imaging
MCR-ALS	Multivariate curve-resolution-alternating least-squares
MLP	Multi-layer perceptron
NMSC	Non-melanoma skin cancer
PA	Photoacoustic
PAI	Photoacoustic imaging
UV	Ultraviolet

Introduction

The idea for this dissertation was conceived at the Department of Ophthalmology in Lund, Sweden, where skin tumors in the eye region are a common and difficult problem for surgeons. Surgeons all over the world lack important information on suspicious-looking skin lesions, including the risk of the lesion being malignant, or the extent of the tumor at, and beneath, the surface. By careful visual inspection and the use of a dermatoscope to visualize the superficial structure of the lesion, an experienced surgeon can make a preliminary diagnosis and excise the lesion, usually using internationally recommended safety margins. This approach sometimes leads to non-radical excision, especially in tumors where the borders are visually unclear (1). This means that all the tumor cells are not removed, and the patient must undergo further surgery. On the other hand, using unnecessarily wide surgical margins can result in complicated and repeated surgeries, with the need for reconstruction and the risk of functional loss or cosmetic deformities.

To prevent excessive removal of healthy skin in sensitive areas such as the eyelids or face, Mohs micrographic surgery, with staged resection and histopathological examination of tumor borders, is commonly used when removing non-melanoma skin cancers (NMSCs). For high-risk facial basal cell carcinomas (BCCs) and for cutaneous squamous cell carconomas (cSCCs) of the head and neck, the recurrence rate is lower with Mohs micrographic surgery compared to standard surgical excision (2, 3). However, the procedure is time- and resource-consuming, and requires specially trained staff (4, 5). To overcome these problems, several imaging techniques for preoperative diagnosis and tumor delineation have been explored in recent years. However, no imaging technique has gained widespread clinical use due to technical limitations.

High-resolution optical techniques, such as reflectance confocal microscopy, can aid the clinician in diagnosing the tumor type (6), however, the field of view is usually very small, and these techniques cannot easily provide volumetric measurements of the tumor. Optical scattering in tissue, which is considered a highly turbid medium, limits the penetration depth of photons (light) to ~1 mm in skin, which is the mean distance light can travel in its original direction before scattering distorts its traceable path (7). Since skin tumors are often thicker than 1 mm, purely optical techniques are seldom used to delineate the deep margins of the tumors. Single-wavelength optical techniques provide detailed images of morphological features in skin, but the interpretation and recognition of tumor

features are subjective and depend on the experience of the user. Optical coherence tomography (OCT) is one of the most promising new techniques for skin tumor diagnostics, but since it is a technique that relies on scattering, its imaging depth is limited to approximately 1.5 mm (8). Also, the limited spectral information provided by OCT prevents analysis of the molecular composition of the tissue. Ultrasound scatters approximately 100-1000 times less than optical waves (7), but also lacks molecular contrast (9) and therefore cannot, for example, differentiate hypoechogenic skin lesions from surrounding hypoechogenic tissues such as fat (8). Therefore, in order to delineate skin tumors to guide surgery, imaging techniques capable of generating molecular contrast at a few mm depth are desired. The aim of the work presented in this dissertation was to explore and develop new spectral techniques for imaging and delineating skin tumors that could help guide surgical excision in the future.

In multispectral and hyperspectral imaging methods, the skin is illuminated with several wavelengths, providing molecular contrast. The spectral data obtained with these methods offer the opportunity of using algorithms that can automatically separate tumor-resembling signals from the signals of healthy skin, providing user-independent information on tumor borders and dimensions.

Photoacoustic imaging (PAI), often also referred to as as multispectral optoacoustic tomography, is a new imaging technique that penetrates deeper into skin than other optical techniques through light-induced generation of ultrasonic waves. PAI therefore has the potential to image both the superficial and the deep borders of skin tumors, while maintaining high resolution. Hyperspectral imaging (HSI) is a spectral technique with a limited penetration depth, but with high resolution. HSI has the advantage of measuring continuous spectral bands, providing detailed information on tumors and healthy skin that can be used for imaging and delineation of superficial tumor borders.

Skin anatomy

The human skin is made up of layers originating from both the ectoderm and mesoderm (10). The epidermis is the most superficial layer, consisting mostly of keratinocytes. Keratinocytes are developed from stem cells in the basal cell layer in the epidermis and produce keratin and lipids that protect the skin from water and exposure to harmful substances or trauma. The thickness of the epidermis in humans varies considerably between different anatomical regions, from approximately 0.05 mm in the thin facial skin, to 1 mm on the heel (11). Melanocytes are another type of cell found in the epidermis; they are located in the basal cell layer and distributed among the keratinocytes. Melanocytes produce melanin, a pigment that is distributed to the keratinocytes, which protects the skin from the effects of ultraviolet radiation. The production of melanin is also

responsible for differences in skin color (11). In dermatology, the Fitzpatrick scale is used to classify skin types based on their tolerance to sunlight, which is related to the amount of melanin in the skin (12). The Fitzpatrick skin type was recorded in this dissertation, since it is expected that the spectral signal of healthy skin will vary depending on the skin pigmentation, as well as other factors such as anatomical location, age, smoking, temperature, etc.

Beneath the basal cell layer of the epidermis is the second skin layer, the dermis, which is approximately 1 mm thick (13). The dermis consists of two layers of connective tissue; the loose, thin, upper papillary layer, and the thicker, dense lower reticular layer. The dermis contains hair follicles, sweat glands, muscles, sensory neurons, and blood vessels. The major component of the dermis is collagen fibers, produced by fibroblasts. The deepest layer of the skin is the subcutaneous layer (hypodermis). It is mainly composed of loose connective tissue and lipid-containing cells, acting as a layer of insulation for internal organs and muscles (11). The thickness of the subcutis ranges from 1 to several mm, depending on the body site and body composition (13).

Skin tumors and their treatment

Skin tumors are divided into benign, pre-malignant and malignant lesions. Tumors can derive from all three layers of the skin, although the most common benign and malignant skin tumors derive from the keratinocytes and melanocytes of the epidermis (Figure 1). Skin tumors usually have a characteristic appearance that can aid the clinician in differentiating between different types of tumors and evaluating the risk of malignancy. However, excision followed by histopathological examination of the tumor are usually necessary to establish the diagnosis. The term ‘nevus’ is broad and is used for a range of both congenital and acquired benign skin tumors originating from different skin layers and cells. Melanocytic nevi are the most common benign tumors, consisting of a local cluster of melanocytes derived from the epidermal basal layer. Malignant skin tumors are broadly divided into melanoma and NMSC. NMSC is a group of malignant tumors consisting of the two main types BCC and cSCC, as well as rarer types (14). BCC and cSCC are the most common malignant tumors of the skin. Malignant melanoma is the third most common skin cancer worldwide and is also the most lethal (15).

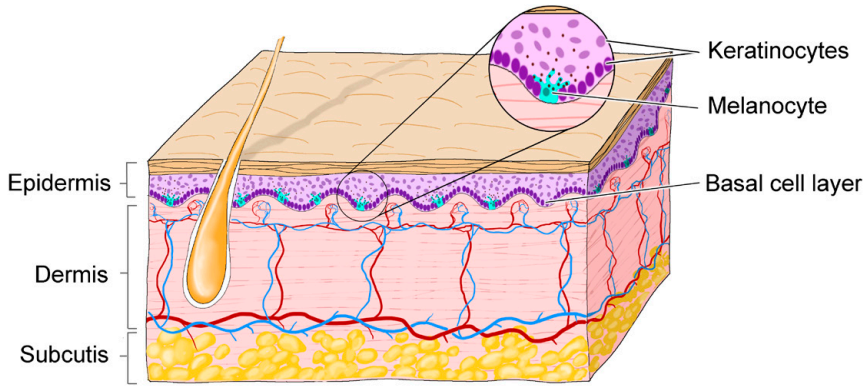

Figure 1. Skin layers and cells.
The epidermis is the most superficial skin layer and contains cells that can undergo carcinogenesis and develop into common skin cancer types. Basal cell carcinoma develops from basal cells in the basal cell layer; squamous cell carcinoma develops from keratinocytes, and malignant melanoma develops from melanocytes. (Illustration by the author.)

Basal cell carcinoma

Basal cell carcinoma develops from basal cells in the deepest layer of the epidermis. In contrast to cSCC, BCC does not have a precursor lesion (16). Risk factors include age, fair skin, and ultraviolet exposure, explaining why BCCs are most often located on sun-exposed areas of the skin (17). BCCs grow slowly and invade tissue locally, and very rarely metastasize (18). Different classification systems are used, according to clinical appearance and histopathological features such as the local invasiveness. BCCs can be treated in various ways, including surgery, curettage, cryotherapy, and photodynamic therapy. The risk of recurrence of a primary (previously non-treated) BCC is up to 10%, whereas the risk of recurrence of a previously treated BCC is up to 30% (19). Recurring BCCs have a more aggressive growth pattern and can cause extensive tissue defects (20). A prospective study of 1214 primary BCCs in Australia revealed that 11.2% were incompletely excised, highlighting the need for thorough preoperative margin assessment. For primary BCCs, a European guideline from 2023 recommends excision with a 3-5 mm safety margin depending on the risk profile of the tumor, down to a depth of the mid-subcutaneous adipose tissue, or by Mohs micrographic surgery in the case of high-risk BCCs (21).

Cutaneous squamous cell carcinoma

Cutaneous squamous cell carcinoma arises from keratinocytes in the epidermis, and is the second most common cancer type in Sweden (BCCs excluded) (18). Risk factors that predispose to the development of cSCC include fair skin, age, ultraviolet exposure, immunosuppression, human papilloma virus, chronic scarring conditions, familial cancer syndromes, and environmental exposures (22, 23). These tumors commonly arise in sun-exposed areas of the skin such as the face, scalp, and dorsal hand (22). An Australian, prospective study from 2007 reported that 6.3% of primary cSCCs were incompletely excised (24). Other studies have reported an overall rate of 8-16% incompletely removed NMSCs, with the remaining tumor most often found at the lateral margin (25). In contrast to BCCs, cSCCs are more prone to metastasize. Early diagnosis and excision are therefore important for the patient's prognosis. New European guidelines (26) recommend the treatment of suspected low-risk cSCC (diameter <2 cm) by excision with a 5 mm margin, whereas suspected cSCCs with high risk factors (including tumor diameter >2 cm, histopathological thickness >6 mm, immunosuppression, ill-defined borders, location in chronic wounds or burns) should be excised with a 6-10 mm margin or by Mohs micrographic surgery.

Malignant melanoma

Malignant melanoma is the most aggressive of the most common skin malignancies and develops from epidermal melanocytes in the basal cell layer. Melanomas confined to the epidermis are defined as melanoma *in situ* or lentigo maligna, whereas invasive melanomas are melanomas that have breached the basal cell layer. The incidence of malignant melanoma in Sweden has has increased more than 5-fold since the 1970s, with more than 5000 new cases diagnosed in 2022 (27). New therapies such as tyrosine kinase inhibitors and immune checkpoint inhibitors have improved the prognosis for metastatic melanoma, however, the survival rate remains poor (28). The clinical appearance of a melanoma is often a pigmented, macular, or nodular lesion >6 mm in diameter, that is sometimes ulcerated (11). Malignant melanoma is divided into 4 types depending on the growth pattern; superficially spreading, nodular, lentigo and acral (on palms and foot soles). Lentigo maligna melanoma is particularly difficult to delineate clinically and therefore has a high rate of recurrence (29). The histopathological diagnosis of melanomas is complicated and often requires methods that can detect molecular pathology (30). There are several risk factors for melanoma, including ultraviolet exposure, previous skin cancer, the number and size of existing nevi, fair skin, and genetic factors (30). Suspicious melanoma-looking lesions should be excised *in toto* with a margin of 2 mm for histopathological examination (diagnostic excision) (30). If the lesion is confirmed to be a melanoma, a second, wide local excision is performed around the site, with

a margin width depending on the histopathological determined tumor thickness. The American Joint Committee on Cancer staging system is the most widely accepted classification and staging system for melanomas (31). In this melanoma staging system, the melanoma thickness is the most important parameter in primary tumor staging (31), guiding clinical management. Swedish and European guidelines recommend wide local excision using a safety margin of 5 mm for melanomas *in situ*; 10 mm for melanomas ≤ 2.0 mm thick, and a 20 mm margin for melanomas >2.0 mm thick, and that all excisions, both diagnostic and wide local excisions, should be made down to the subcutaneous fat (30, 32). A sentinel lymph node biopsy is recommended for primary melanomas thicker than 1.0 mm (30). Some melanomas, for example melanomas located on the face, are difficult to excise with the above recommended wide local excision margins, due to the risk of cosmetic or functional damage. Partial biopsies are not recommended due to the risk of misdiagnosis and inaccurate staging (30).

Histopathologic examination

Histopathologic examination is the gold standard technique for the diagnosis of skin tumors. After excision, the tissue is placed in aqueous formaldehyde for fixation, which takes approx. 6-24 hours depending on the lesion size (33). At the laboratory, the tissue is cut to size in vertical cross-sections and then processed based on histology protocols, usually involving ethanol baths and paraffin infiltration. The tissue is then cast in a paraffin block and sectioned using a microtome, resulting in sections of approx. 4 μm in thickness (34). Finally, the sections are stained with hematoxylin and eosin (and sometimes also elastica-van Gieson stain and periodic acid-Schiff stain), visualizing different molecular structures. Immunohistochemical techniques using fluorescence labelled antibodies are used when diagnosis of a lesion cannot be made using other staining techniques (35). Using histologic criteria, the pathologist assesses the sections using a microscope and reports the findings including the diagnosis, the thickness of the tumor (not required for BCC) and measurements of the tumor-free margins. For melanocytic tumors, weighing histologic criteria as regards to malignancy is however difficult and requires long experience (35).

Mohs micrographic surgery

Mohs micrographic surgery is a surgical technique designed to minimize the loss of healthy skin. It is commonly used to treat high-risk BCC and cSCC in cosmetically or functionally sensitive areas such as the head and neck (36). A growing number of studies suggest that Mohs micrographic surgery is also safe for the treatment of melanoma without the need for a wide local excision (37). The technique is performed by excising the tumor close to its clinically visible border,

including deep tissue. The tissue is then frozen, sectioned, and examined under a microscope to determine whether all the tumor cells have been removed (37). If the examination reveals residual tumor cells at the margin, excision is extended at the corresponding site until the excised tissue is clear of tumor cells (38). This not only prevents extensive loss of healthy skin, but also removes the need for a second surgery. Unfortunately, this procedure is time consuming, costly, and requires specially trained staff (39), which limits its widespread use. Due to the softness of the tissue, cutting during surgery is difficult and more prone to artifacts than sectioning of formalin-fixed tissue (35). Interpretation of the frozen sections is also considered more difficult than interpreting permanent, fixed sections (37). Our group has previously described a case of a BCC on an eyelid, in which PAI of the tumor was performed on the freshly excised and unfixed tumor immediately after surgery. The resulting 3D image showed that one of the edges was not clear of tumor cells (40), which was later confirmed by histopathology. This finding indicates the potential of PAI for use during Mohs surgery, which would avoid the need for freezing and sectioning during the surgery, as well as the need for specially trained staff.

Non-invasive techniques for skin tumor imaging

To minimize harm to the patient, diagnostic techniques should be both non-ionizing and non-invasive. Apart from differentiation between benign and malignant skin lesions, several different non-invasive techniques have been used in attempts to image and delineate skin tumors. However, they have not gained widespread clinical use for the purpose of preoperative margin delineation due to various limitations. Descriptions of some of the most studied techniques and their limitations are given below.

Dermatoscopy

Dermatoscopes are used widely by dermatologists, plastic surgeons, and primary care physicians to examine skin structures and patterns. The commonest hand-held dermatoscopes illuminate the skin with polarized light (where the electric field oscillates in a defined plane) or non-polarized light (where there is no defined plane for the electric field) with a 10x magnification (41). By using polarized light, dermatoscopes can block reflected light from the most superficial layer of the epidermis (stratum corneum), which enables better visualization of subsurface structures in the epidermis and superficial dermis. As it is a subjective modality, it requires trained and experienced users to obtain reliable results (42). The primary objective of dermatoscopy is to improve diagnostic accuracy, especially of early melanomas (41). Dermatoscopy is the most widely used clinical technique for

superficial tumor border assessment, but only a few studies have evaluated its accuracy for this purpose. One study showed that while dermatoscopy has a high accuracy for BCC diagnosis and subtype classification, its accuracy in superficial tumor border assessment of several subtypes of BCC was limited (43). Another study comparing dermatoscopy to visual inspection of superficial tumor borders of infiltrative BCCs showed no difference in the final number of stages used in Mohs micrographic surgery (44). For lentigo maligna and lentigo maligna melanoma, a study showed that 11 out of 32 lesions still had positive margins following primary excision after visual inspection with dermatoscopy (29).

Optical coherence tomography

Optical coherence tomography creates cross-sectional images of skin with a larger penetration depth than many other purely optical imaging technologies. The images derive from interference signals received from the skin and a local reference. The technique has a maximal penetration depth of up to 2 mm, and the axial resolution is 5-10 μm, making it a promising tool for skin tumor diagnostics, although the field of view is somewhat limited (6x6 mm), and the penetration limit makes it unsuitable for the assessment of deep tumor borders in infiltrative tumors (45, 46). Newer types of OCT (spectral domain and swept source OCT) employ spectral light sources, but in a very narrow spectral range, which strongly limits the molecular contrast. The results of studies on the potential of optical coherence tomography in assessing tumor borders in NMSC are conflicting, with some studies reporting good accuracy (47, 48) and others low accuracy (49), possibly due to misinterpretation of glands and vessels, as well as the limited penetration depth. Studies on optical coherence tomography for lateral margin assessment of melanomas are lacking.

Reflectance confocal microscopy

In reflectance confocal microscopy, a low-power infrared laser is used to illuminate the skin, producing grayscale, horizontal (parallel to the skin), high-resolution, histopathology-resembling images with an approximate 0.5x0.5 mm field of view. Automated software can combine consecutive sections in one plane, producing a mosaic image with a field of view of up to 10x10 mm (50, 51). Studies have shown that the technique improves the diagnostic accuracy of melanomas and NMSCs (52-54). Unfortunately, due to a decrease in resolution with depth, diagnostic interpretation is limited below a depth of 100-150 μm, which may be insufficient to detect tumor invasion or deep tumor borders (50). Nodular tumors or tumors with epithelial thickening, ulceration, or hyperkeratosis may also be difficult to image adequately as these factors reduce the image quality (50). Reflectance confocal microscopes are difficult to use for superficial tumor

border delineation as the images must be acquired in a closed chamber, which obscures the tumor. Hence, the images produced with cellular resolution cannot easily be precisely located on the skin (55). To circumvent this, one group marked *the angles* of a small skin area with a pen and correlated dermatoscopy images of 37 lentigo maligna and lentigo maligna melanoma to reflectance confocal microscopy images in 4 directions. In 17 of the patients, the images revealed suspected tumor features more than 5 mm beyond the dermatoscopy border, which led to changes in the management of the patients (56). Other groups have used dermatoscopy-guided cuts or biopsies to guide the location of reflectance confocal microscopy images in ill-defined BCCs and lentigo maligna melanomas (55, 57, 58). A major limitation of the technique is that imaging relies on the reflectance of a single illumination wavelength, limiting the contrast between light-absorbing molecules (59). Hence, the differentiation of benign and malignant tissue relies on the recognition of morphological features in the images and is therefore dependent on the dermatopathological experience of the user (60, 61). Furthermore, benign and malignant tumors share some morphological features, and can therefore be difficult to differentiate, even for experienced dermatologists (62). The time required to image a whole skin lesion varies from several minutes up to an hour, depending on the size and complexity of the lesion (60). Assessment by an expert then takes approximately 5 minutes per 8x8 mm mosaic image (56). The total time used for imaging and assessment makes the technique difficult to use in the clinical setting.

High-frequency ultrasound

High-frequency ultrasound is performed at a sound frequency of 20-100 MHz. Although it cannot be used to image deep organs it is suitable for skin imaging, where it can achieve penetration of up to several mm. It has been reported that measurements of Breslow's depth in melanoma with high-frequency ultrasound showed good correlation to values obtained histopathologically (63). With the technique, both melanomas and NMSCs appear hypoechogenic, surrounded by the more echogenic epidermis and dermis. Given that most skin tumors are hypoechogenic, high-frequency ultrasound is mainly used for anatomical assessment of skin tumors including tumor thickness and infiltration, and cannot distinguish between inflammatory infiltrates, melanocytic proliferation, and neovascularization (63).

Other techniques

The 3D imaging techniques magnetic resonance imaging and diffuse optical tomography are limited by low spatial resolution, the smallest details observable being about 0.5 mm (64). A recent development of magnetic resonance imaging,

called high-resolution magnetic resonance imaging, has a spatial resolution of up to 100 μm and could potentially be used for structural imaging of skin, but cannot provide molecular contrast without the use of exogenous contrast agents. Two small studies have shown that high-resolution magnetic resonance imaging with exogenous contrast agents combined with a microscopy surface coil could delineate different skin layers down to the muscle fascia and predict NMSC and melanoma borders with good correlation to histopathological results (65, 66).

Spectral imaging

Most imaging techniques today are based on electromagnetic radiation (light), which interacts with tissues differently depending on the wavelength. Gamma rays and X-rays in the short wavelength range have high energy and are ionizing, which means they can alter molecules and are potentially carcinogenic. So-called optical imaging encompasses ultraviolet, visible, and infrared light, and is considered non-ionizing. Ultraviolet light is used to target DNA and RNA absorption in cell nuclear imaging (67), but can cause chemical reactions and damage of DNA, which limits its clinical use.

Naturally occurring light-absorbing molecules are also known as endogenous chromophores. In techniques using single-wavelength excitation, the optimal excitation wavelength is chosen based on known chromophore absorption features. The resulting images will show differences in light absorption for the same wavelength but cannot discriminate between different chromophores. This is especially problematic in skin imaging, since both melanin and hemoglobin are strong chromophores, making it difficult to target other molecules. In analogy to ultrasound or X-rays, single-wavelength imaging will therefore reveal morphological rather than physiological or cellular features.

Spectral imaging uses multiple wavelengths to illuminate tissue. The resulting emitted signals are related to the molecular constituents of the illuminated tissue, which makes spectral imaging relevant for imaging of skin tumors. Due to the high absorption of visible light by blood and the high absorption of infrared light by water and lipids, light penetration in biological tissues is deepest in the near-infrared region. The near-infrared region lies between the visible region and the infrared region in the electromagnetic spectrum (Figure 2). Exogenous contrast agents, such as nanoparticles, organic dyes, and proteins, can be designed to bind to certain molecules and provide strong contrast at specific wavelengths, which maximizes their detection (68). However, they must be injected and are therefore invasive to the patient. Endogenous chromophores, such as blood, melanin, lipids, and water (Figure 3), also provide contrast, but do not affect the biological environment.

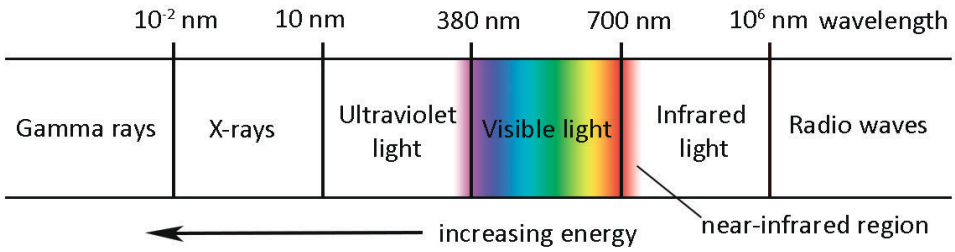

Figure 2. The electromagnetic spectrum.
The shorter the wavelength, the higher the photon energy. The near-infrared region lies between wavelengths of approximately 700 and 2500 nm. (Illustration by the author.)

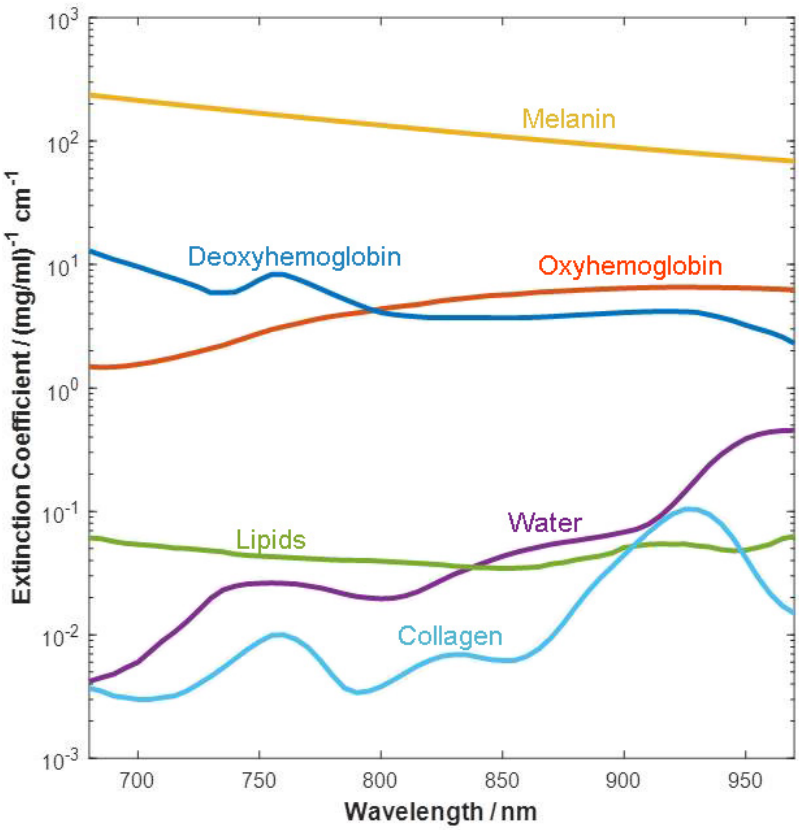

Figure 3. Light absorption of endogenous chromophores in the 'optical window'.
The figure illustrates the relative absorbance of endogenous chromophores in the spectral range 680-970 nm (the 'optical window') in terms of the extinction coefficient (a measure of how strongly the chromophores absorb light at a particular wavelength), assuming equal concentrations and light propagation lengths. Reproduced from data in S. L. Jacques (69) using MATLAB R2017b (MathWorks Inc., Natick, MA, USA).

Photoacoustic imaging

Purely optical imaging methods do not have sufficient penetration depths to visualize all layers of the skin, or skin tumors thicker than 1.5 mm. PAI is a new multispectral (several preselected wavelengths are used) technique that records light-induced sound waves from tissue. Because sound waves scatter less than light waves, the technique can penetrate skin up to several mm while maintaining a high resolution. These features make PAI a potential tool for the imaging of skin tumors. Figure 4 shows approximate maximal penetration depths for various imaging techniques.

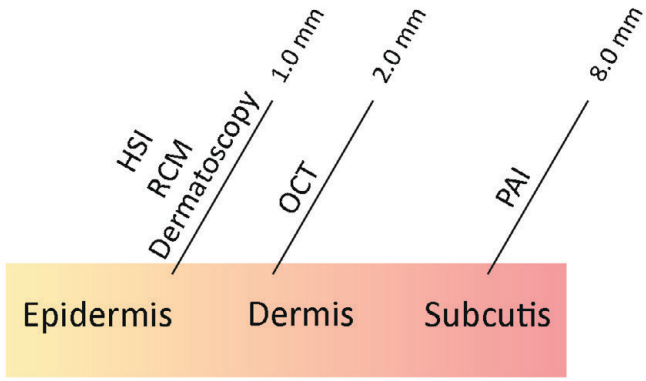

Figure 4. Penetration depths in skin for various imaging techniques.
The maximum approximate penetration depths for HSI, RCM, Dermatoscopy, OCT and PAI in the three skin layers; epidermis, dermis and subcutis. (Illustration by the author.)

PAI derives from the discovery of the 'photoacoustic effect' by Alexander Graham Bell in 1881. As the name implies, Bell found that light could be converted into sound by exposing substances to intermittent sunlight (70). A century later, the introduction of lasers allowed for signal improvement, which made it possible to explore the photoacoustic effect in biomedical research (71). Improvements in ultrasonic detectors, data acquisition times, and data processing have made PAI an increasingly interesting technique for biomedical imaging (72), especially in the field of cancer research.

An *in vivo* study on 31 patients with breast cancer showed that PAI could image the tumors with high contrast, providing reasonably good tumor size estimates (73). PAI depths of 4 cm have been reported *in vivo* in humans without the use of contrast agents (74). Although most research on PAI in humans has been carried out on breast cancer, one of the most promising areas for PAI is probably skin cancer, where light attenuation is less pronounced than in the breast. Here, it has the potential to visualize the entire extent of a skin tumor with optical contrast,

thereby filling the gap between existing optical techniques for superficial tumor characterization and the structural, deeper images provided by ultrasound.

PAI is based on the emission of nanosecond pulses of laser light that are absorbed by chromophores in the tissue. Absorption of the energy from a laser pulse, and the subsequent heat release of that energy into the environment of the chromophore causes a short local expansion of the tissue, resulting in a small pressure wave, i.e. a sound wave is emitted. The pressure wave is recorded by an acoustic detector and converted into an electrical signal by piezoelectric sensors in the detector. In the photoacoustic detector used in the studies described in Papers I-III, the piezoelectric sensors are arranged in a linear array, producing a rectangular field of view. Linear array acoustic detectors are inexpensive, handheld, and can easily be integrated with light sources and conventional ultrasound systems (75). The spatial resolution of a linear transducer array represents the resolution along three separate axes; the lateral, the elevational, and the axial, as shown in Figure 5.

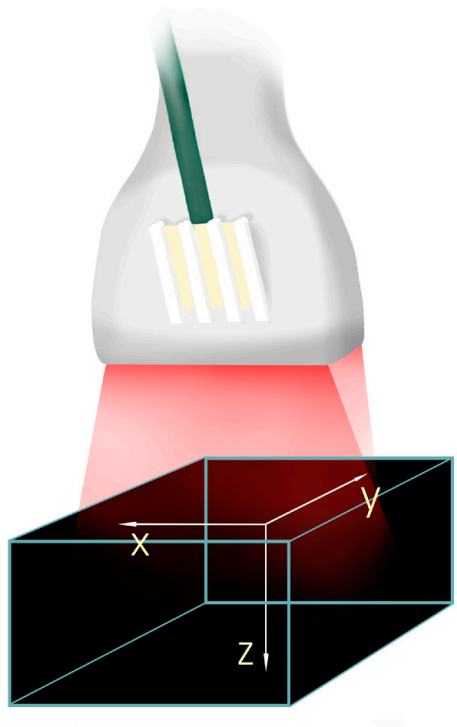

Figure 5. Imaging axes.
The three perpendicular imaging axes x, y and z. x is the lateral axis, y is the elevational axis and and z is the axial axis. The PA transducer captures 2D images in the cross-sectional xz-plane. By moving the transducer along the elevational y-axis, multiple 2D-images can be aligned to form a 3D image. (Illustration by the author.)

The lateral resolution (along the x-axis) is defined by the distance between the piezoelectric sensors in the array, and the axial resolution (along the z-axis) is defined by the center frequency of the transducer. For volumetric PAI, the linear array transducer is moved along the y-axis, capturing 2D images that are then aligned to form a 3D image. Due to the fixed cylindrical focus of the piezoelectric sensors, the elevational resolution is significantly lower than the axial and lateral resolutions (76). The spatial resolution in PAI decays with increasing depth from around 100 to 400 μm due to acoustic attenuation and distortion (77, 78). The higher the center frequency and the bandwidth of the acoustic detector, the higher the spatial resolution, but the lower the penetration depth. For example, an acoustic detector with a center frequency >20 MHz provides a sub-100 μm lateral resolution with an imaging depth of several mm, whereas a detector with a center frequency of <10 MHz has lower resolution, but the penetration depth is >10 mm (76). Spherical or cylindrical detectors can also be used in PAI systems (79).

The ability of PAI to detect and delineate deeper-lying tumors can be enhanced by exogenous contrast agents (80, 81). Exogenous contrast agents can provide high contrast when the endogenous optical contrast is not sufficient, which is especially desirable in the near-infrared window, where deep tissue imaging is achievable at the expense of endogenous contrast (81). For example, gold nanoparticles have been used in conjunction with hormones and antibodies to target melanomas and squamous cell carinomas in mice (82, 83). Some organic dyes, such as methylene blue and indocyanine green, are approved for human administration and have shown strong PA contrast in both animal and human studies on sentinel lymph nodes (84-86). However, there are no long-term studies of biological distribution, cytotoxicity, or renal clearance of exogenous contrast agents with targeting ligands exposed to PA light (87), and so far, all *in vivo* human PA studies on skin tumors have been carried out without exogenous contrast agents.

PAI systems can be broadly divided into optical (PA microscopy) and acoustic resolution (PA tomography) systems. In PA microscopy, which is mostly used for preclinical studies (88), focused laser light is used for high-resolution imaging (~5–50 μm) at shallow depths (up to 1 mm). In PAT, diffuse laser light is used for deeper imaging (several mm), at the expense of the resolution (~100–500 μm).

Previous animal studies using PA microscopy and PA tomography have imaged the capillary bed (89), tumor angiogenesis (90, 91), and xeno-transplanted melanomas (91-95). Previous PAI studies on human skin tumors have been small and limited to a few tumors or some tens of tumors at most. Among the benign tumors studied are pigmented nevi (96-100), vascular tumors (101-104), seborrheic keratosis (97, 105, 106), viral wart (107), and neurofibroma (100). Malignant skin tumors studied with PAI include BCCs (40, 104, 106, 108-110), cSCCs (106, 108), and malignant melanomas (97, 111-113). There are considerable methodological differences between these studies. Many were pilot studies of new PA systems, where a few tumors were included to demonstrate the

imaging potential of the new system (96-99, 102-104, 109, 111, 113, 114). Other studies have used commercially developed PAI/ultrasound systems for the characterization of different types of tumors, or to evaluate PAI in a clinical setting (40, 101, 105-107, 110, 112). In this dissertation, the term PAI refers to PA tomography (Papers I-III).

Melanin and hemoglobin are the most common molecular targets in previous studies. PAI has been shown to be able to visualize vessels and blood volume inside, or in the vicinity of, tumors by measuring hemoglobin absorption (98, 100, 102, 107, 108, 111), as well as hemoglobin concentration and oxygen saturation in vascular tumors (101). Malignant tumors typically have a dense and unorganized vasculature compared to benign tissue (115), making increased hemoglobin content a potential indicator of malignancy. Visualization of the capillary bed is possible using PA microscopy to detect hemoglobin absorption (102), whereas broader feeding vessels can be visualized with PA tomography (111). Melanin absorption has been used for delineation and measurements of tumor dimensions in pigmented tumors (98, 105-107, 111, 112), showing good correlation with histopathological measurements in studies where these were available. A more recent approach to PA skin tumor imaging has been to obtain the spectral fingerprint of a tumor using several excitation wavelengths, and then to use the tumor spectrum (as opposed to known chromophore spectra) in spectral analysis for tumor pixel identification (97). This type of approach was used in all the studies presented in this dissertation.

The Union for International Cancer Control classification system for skin cancer describes the primary tumor size and features (T), regional lymph node involvement (N) and presence of distant metastatic spread (M). Early and correct classification of a cancer according to the TNM system could improve patient management and prognosis. Studies on melanoma have shown that PAI has the potential to aid in the identification of sentinel lymph nodes (85, 86, 116-119), which is the first site of metastasis, and to detect melanocytes in the bloodstream (120-124).

PAI takes advantage of the fact that each endogenous chromophore in the human skin has its own, unique light-absorbing spectrum, which can be used for functional monitoring and imaging. To understand this, one can consider the well-known finger pulse oximeter, which is used in health- and emergency clinics worldwide (Figure 6). In this device, differences in the absorption spectra of oxygenated and deoxygenated hemoglobin are used to monitor oxygen saturation in sick patients.

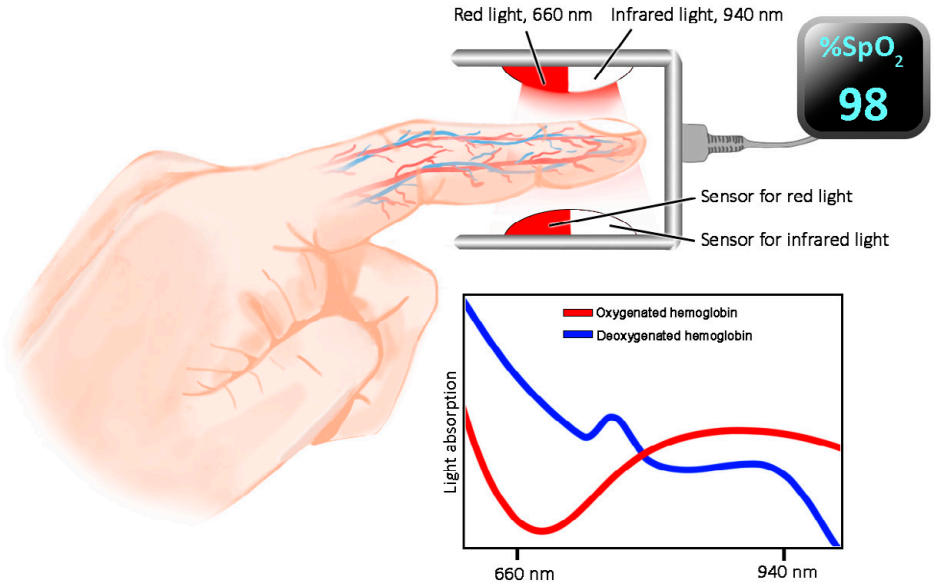

Figure 6. Principle of a pulse oximeter measuring hemoglobin light absorption.
The commonly used pulse oximeter serves as an example of how the absorption spectrum of tissue chromophores such as hemoglobin can be utilized for content quantification. The skin is illuminated with visible red light (660 nm) and infrared light (940 nm). The absorption of light at these wavelengths differs between oxygenated (red) and deoxygenated (blue) hemoglobin, which results in more visual, red light passing through oxygenated hemoglobin and more infrared light passing through deoxygenated hemoglobin. The percentage oxygen saturation can then be estimated through measurements of the transmitted light and calculation of ratio. (Illustration by the author.)

The use of multiple excitation wavelengths in PAI produces images of tissue in which each single pixel contains a unique spectrum representative of the molecular composition at that location (Figure 7). The spectrum in one pixel can be assumed to represent a combination of spectra from several chromophores. To estimate the contribution of a specific chromophore or component to the pixel spectrum, spectral analysis is needed.

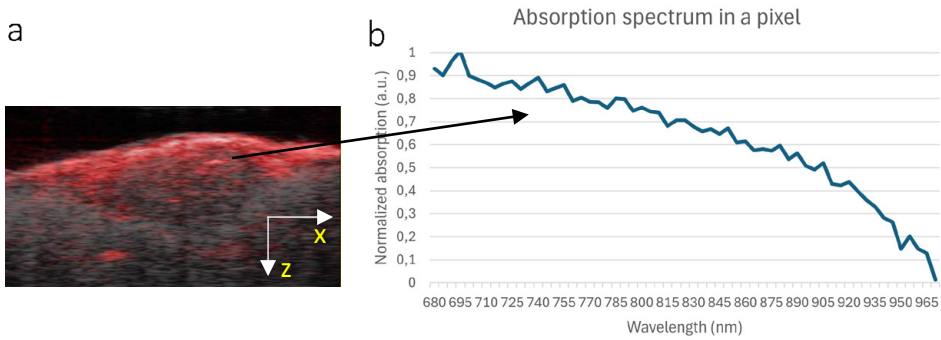

Figure 7. Example of a PA absorption spectrum in a single pixel.
Live screenshot during a 2D PA scan showing light absorption in red overlaid on an ultrasound image of the same cross section (a). Each 2D cross-section is illuminated with 59 different wavelengths of light, and hence, each pixel in the PA image will contain an absorption spectrum, as shown in the graph (b).

In this work, a combined PAI/high-frequency ultrasound system was used to obtain skin tumor spectra for imaging and delineation of the tumors in 3D. The ultrasound images provide an anatomical and structural reference for the PA images. PAI has also been combined with other imaging modalities, such as OCT (104).

Hyperspectral imaging

Hyperspectral imaging (HSI) is an optical, non-invasive imaging technique, in which reflected light is analyzed over a broad wavelength spectrum in every pixel. HSI has existed for a few decades but has only recently been developed for the purpose of biomedical imaging. HSI has the advantage of generating very detailed spectral information from the superficial skin layers (depth up to 0.2 mm) at high speed and with a large field of view. While conventional cameras capture light in three spectral bands (red, green, and blue), HSI employs hundreds of contiguous spectral bands (125) (Figure 8). As in PAI, tissue chromophores such as melanin, hemoglobin, proteins, and water, affect the absorption and reflection of emitted light, creating a unique spectral signature for different tissues. A hyperspectral image can be generated in different ways. A detailed description of the different HSI techniques has been presented by Lu & Fei (126). In medicine, HSI has been used to study a wide range of diseases, including cardiac disease (127), diabetes (128), burn wounds (129), and different types of cancer (130, 131). In skin cancer, HSI has shown promising results as a diagnostic tool for discriminating between benign and malignant pigmented lesions (132-136), tumor invasiveness (137), and tumor delineation (138-140). HSI has the advantage of a large field of view, and images can be interpreted quickly without histopathological experience. However, only a few small studies have used HSI for skin tumor delineation.

In the present work, HSI was used in combination with machine learning for the delineation of different skin tumors on the skin surface. In HSI, scanning a single tumor generates several gigabytes of spectral data. Although this may pose a problem for data storage, it provides good opportunities for machine learning, where large training datasets are needed.

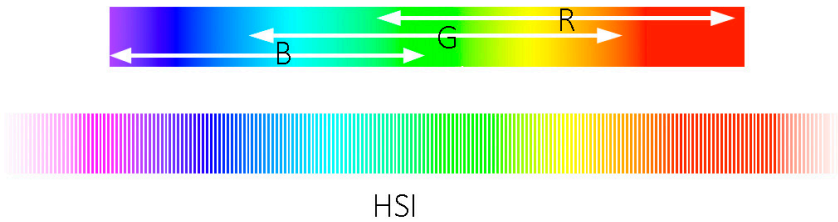

Figure 8. Spectral bands.
A simplified figure illustrating the difference between the number of spectral bands employed by conventional cameras and HSI. Conventional cameras capture light in the three overlapping spectral bands R (red), G (green) and B (blue), whereas HSI captures light in hundreds of contiguous spectral bands. (Illustration by the author.)

Spectral analysis

When imaging tissue in which the exact location of different chromophores is unknown, spectral analysis of the pixels is needed to isolate the chromophores and estimate their relative contributions to the pixel spectrum. This can be done in different ways, for example, using methods based on linear regression- or statistical detection, or by machine learning (artificial intelligence). An introduction to the spectral analysis methods used in this work is given below.

Linear spectral unmixing

One of the most common methods of spectral analysis is linear spectral unmixing. In linear spectral unmixing, it is assumed that the spectrum measured in each pixel is a linear combination of spectral signatures belonging to set of different chromophores, weighted by their relative abundances. Usually, the spectra from known chromophores are used in the algorithm, such as those for blood, water, and melanin (69). However, unknown target spectra can also be incorporated into the algorithm, such as a presumed tumor spectrum, or the spectrum of presumed healthy skin, to calculate the fractional abundance of the tumor spectrum or healthy tissue spectrum in a pixel. A drawback with the method is that it only accounts for target spectra that have been included in the algorithm, and hence, there is a risk that contributions from other chromophores can be missed. In this

work, linear spectral unmixing was applied to PA data to identify pixels with tumor-resembling spectra (Papers I-II).

Adaptive matched filter

The adaptive matched filter (AMF) is a method of spectral unmixing that estimates the probability of each pixel being in the target area based on the statistical characteristics of the background. By applying a multivariate Gaussian distribution to model the background, the method accounts for spectral fluctuations due to spectral coloring (wavelength-dependent light attenuation) and additional noise sources (141) . It has been shown that AMF outperforms common linear spectral unmixing algorithms provided the target is sparsely distributed in the tissue (142). Applying AMF to PA images at different wavelengths results in detection images in which the amplitude corresponds to target probability.

Machine learning

Machine learning is a branch of artificial intelligence (Figure 9) in which computer models learn from 'training data' and make predictions of data that they have not seen before by identifying patterns in the data (143). An important use of machine learning is in so-called classification problems, where objects belonging to different categories are separated by the machine learning model. The training data for the model are therefore labelled data points belonging to the different categories. So-called Artificial neural networks (ANNs) were used as the machine learning models in Paper IV. ANNs are models that are inspired by the signal propagation between neurons in the human brain. In an ANN, nodes receive input signals that are weighted according to how important they are for the output. The information is then combined and processed through an activation function to produce a signal, which is then forwarded to the next layer of nodes in the ANN. In a multi-layer perceptron (MLP) ANN, several layers of nodes allow for more complex learning. The process by which an MLP learns is called the backpropagation algorithm. Simply explained, backpropagation means that a supervisor corrects the ANN when it makes mistakes, and the error is propagated back to the previous layer, leading to an adjustment of how inputs are weighted. Hence, the ANN will learn from both the labelled data and from its mistakes.

One problem associated with MLPs is that the more layers are added, the more difficult it becomes to update the weights because the signal becomes weaker. Deep learning models such as convolutional neural networks (CNNs) seek to overcome this 'vanishing gradient' by detecting features that are considered good input for the MLP. CNNs are commonly used for detecting and classifying objects in images. Here, CNN works like a filter that moves over the image and extracts

features from one neighboring part of the image at a time, and then connects all the information.

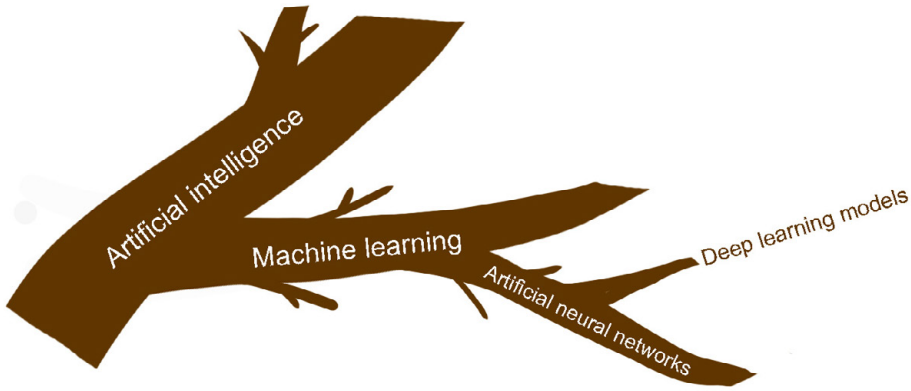

Figure 9. Branches of artificial intelligence.
ANNs and deep learning models such as CNN are branches of artificial intelligence and machine learning. ANNs and CNNs are often used to find patterns and to classify objects in medical images. (Illustration by the author.)

The past decade has seen an explosive increase in the number of studies and publications in the field of artificial intelligence and machine learning. Neural networks are often trained and evaluated using large, public datasets of dermatoscopy images (144, 145). CNN algorithms have been shown to have comparable or superior performance in the classification of both non-pigmented and pigmented skin tumors from dermatoscopy images, compared to clinicians (146, 147).

Segmentation

The purpose of segmentation is to define an object in an image, in this case a tumor. Segmentation divides original images into classes (148) such as tumor or healthy tissue, enabling delineation of the tumor borders. Only a few studies have used ANNs for segmentation of skin tumors using HSI (149, 150). Studies on PAI have shown that neural networks can be used for segmentation of normal skin structures (151, 152), but studies on skin tumors are lacking. Most segmentation studies (usually on dermatoscopy images) have relied on manually drawn ground truth masks for segmentation training, strongly limiting their clinical value. Ground truth masks define the position and size of objects in images. They are usually drawn manually in tumor delineation studies, to serve as reference standards in the training of ANNs. Attempts have been made to improve ground truth images by drawing masks related to histopathological cross sections, but the results were only approximate, affecting both training and evaluation of the network (149). The majority of segmentation techniques for spectral data involve a standard deep learning model called U-net (153). However, training this type of

network requires annotation for each individual pixel, and is therefore difficult to use for preoperative delineation purposes unless the true (histopathological) tumor borders are precisely matched with locations in the training images.

Aims

The general aim of this work was to explore and develop new spectral techniques for imaging and delineation of skin tumors, to guide surgery.

Specific aims

- To explore PAI for 3D delineation of tumor borders, and HSI for 2D tumor delineation on the skin surface
- To explore methods of spectral analysis that can differentiate between signals from tumors and from healthy skin, including linear spectral unmixing, the adaptive matched filter and machine learning
- To develop automatic algorithms for pixel classification and tumor border delineation

Materials and methods

Ethics

The patients were given oral and written information about the study and were informed of the voluntary nature of participation. Emphasis was put on the fact that neither the study nor participation in it would affect their individual treatment or prognosis. Patients younger than 18 years, and patients who were incapable of providing consent were not included in the studies. All the included patients gave their fully informed written consent. The protocols for the studies were approved by the Ethics Committee at Lund University, Sweden, and the Swedish Ethical Review Authority. The research was conducted in accordance with the Declaration of Helsinki 2013 (154). Access to personal data relevant to the studies was approved by the KVB-group, Region Skåne.

The safe handling of the patients and skin lesions was of fundamental importance, since the procedure involved potential risks. The patient safety risks included the risk of laser-induced eye injury, incorrect patient id-labelling or mix-up of lesions, loss or damage to lesions, incorrect handling of histopathology referral documents, and delays in transportation of the lesion to the Department of Pathology. To minimize these risks, laser safety regulations were followed, and step-by-step protocols were developed and then approved by the head of the Department of Dermatology.

One of the ethical difficulties associated with this work is that it involves patients who are dependent on treatment for their skin lesions. Before surgery, the patients were informed about the study, and given the choice to participate. The limited time before surgery could have led to the risk of therapeutic misconception, where the patient might believe that the researcher is involved in the treatment, and therefore agrees to participate, or that the results of imaging will be used for diagnosis directly following surgery. It can also be anticipated that patients who have a suspected malignant skin tumor are more vulnerable and thus prone to participate in research involving the diagnosis of skin tumors.

Another ethical problem associated with this research is that we recorded information about skin type (Fitzpatrick scale), which is sensitive personal data, but nonetheless important since the degree of skin pigmentation affects spectral signals.

Subjects and tumors

All the patients were recruited from the Department of Dermatology at Skåne University Hospital in Lund. Inclusion criteria for all the studies were age ≥18 years and that the tumors were suspected of malignancy and primary excision was planned (i.e. not re-excision). The skin types of the patients varied, but most of the patients had skin type II on the Fitzpatrick scale (fair skin).

In the first study (Paper I), 61 patients with 76 suspected cSCCs were recruited. Three of the tumors were scanned with PAI both *in vivo* before surgery, and *ex vivo* immediately after surgery. The remaining tumors were scanned *ex vivo* only. Almost half of the tumors (37/76) were confirmed by histopathological examination to be cSCCs. The data from the three *in vivo* scans were not included in the analysis due to a large variation in the spectral signal, probably caused by movement artifacts. Four of the *ex vivo* cSCCs were also excluded due to a large variation in the spectral signal (cause unknown). Data from the remaining 33 *ex vivo* cSCCs were thus analyzed.

In the second study (Paper II), 52 suspected melanomas (from 50 patients) were scanned with PAI *ex vivo*. Histopathological examination showed that 25 of the tumors were malignant melanomas and the remaining 27 tumors were nevi. Four of the tumors were also imaged with HSI, and the data is included in Paper IV.

In the third study, (Paper III), data from seven of the *ex vivo* malignant melanomas from the previous study (Paper II) were analyzed with AMF-ATS.

In the final study (Paper IV), 22 skin lesions suspected of being BCCs, cSCCs, or malignant melanoma, in 21 patients, were imaged *ex vivo* with HSI. Four of these tumors had also been scanned with PAI and were included in Paper II. The histopathological diagnosis revealed that three of the lesions were not tumors (sun damaged or bluish colored skin) and these lesions were therefore excluded from analysis. One papilloma was also excluded from the analysis due to its small size, making it difficult to handle during image acquisition. Data from the remaining 18 tumors were analyzed with machine learning. Spectral component maps (images visualizing spectral contrast) of the tumors revealed that four of the tumors (1 cSCC, 2 BCCs, and 1 fibrous histiocytoma) had insufficient signal-to-noise ratio to allow the delineation algorithm to be run reliably and were therefore excluded from the comparison with histopathological measurements.

Safety aspects

The PA system used (Papers I-III) does not have CE or FDA approval for clinical use. It was therefore critical to ensure the safety of all persons in the vicinity of the

system. Aspects of laser, ultrasound, and electrical safety were carefully controlled.

Lasers can potentially damage the eyes and skin and pose a risk when in contact with combustible materials. Eye injuries are the major risk when working with lasers, and therefore the classification of lasers is mainly based on the amount of exposure the eye can be subjected to with only low risk of damage. The PA system used contains a Class IV laser, meaning it belongs to the class of lasers with the highest energy output. Due to the wavelength range used (visible to near-infrared light), it is dangerous, especially to the retina of the eye, where it can cause irreversible burns and lead to vision impairment or blindness. The laboratory and equipment used followed regulations and standards set by Lund University, the Swedish Work Environment Agency, and the Swedish Radiation Safety Authority. Laser safety glasses (LSBGKG-33-BK, Phillips Safety Products, Middlesex, NJ, USA) providing protection in the wavelength range used were worn by all staff, in accordance with the European norm for laser safety eyewear. The three patients whose tumors were scanned *in vivo* (Paper I) wore stainless steel eye shields as long as the PA system was turned on. A comprehensive description of exposure levels with the PA/ultrasound system used, the safety equipment, and electrical safety analysis has been published previously (155).

The other type of laser used in this research, in the HSI system, was a Class I He-Ne laser. Two of these were used for height alignment to obtain the correct distance from the measured surface to the objective lens. This class of laser has a low energy output and is often used in toys, laser pointers, etc., without the need for eye protection. In the HSI system, the light source used to illuminate the tissue surface during measurements was a tungsten-halogen lamp with an output power of 100 W. Since the light was guided through a fiber and the illuminated surface was placed at least 10 cm away from the fiber, an estimated 1 W reached the tumor. Accounting for the illuminated area, the effective photon flux was estimated to 0.1 W/cm^2, which is similar to the solar flux. The lesion surface is therefore heated slightly, but no damage is induced to the tumor or the surrounding healthy tissue.

Experimental setup and equipment

Experimental setup

Following excision by surgeons at the Dept. of Dermatology, the tumors were placed in saline and transported directly by researchers to the research laboratory at the Department of Ophthalmology, Skåne University Hospital, Lund, where the imaging of tumors was carried out. Hair was removed from the tumor and skin before imaging.

For PAI, holding sutures (Prolene 6-0, Ethicon, Cincinnati, OH, USA) were carefully attached, either to existing sutures, or around the excision margins of the tumor-free edges of the lesion, under a microscope, and the tumor was then placed centrally in a 100x70x50 mm Perspex container with balanced salt solution. A layer of black ultrasound-attenuating material was placed in the bottom of the Perspex container. To simulate an *in vivo* setup, in which there must be a distance between the laser fibers and the skin surface, a 10-mm thick transparent gel pad (Aquaflex, Parker Laboratories Inc., Fairfield, NJ, USA) with protective plastic was used (Figure 10). The tumors were centered under the transducer, and a fast ultrasound scan was made along the tumor to control its position and to check that the transducer could move freely without touching the tumor. After PAI, the holding sutures were removed, and the tumors placed in formalin.

No sutures were required for HSI imaging. The tumors were illuminated with white light, and the camera aligned so that the detection line of the sensor was centered under the illumination spot. The tumors were then scanned and, after examination, placed in formalin.

After imaging, the tumors were transported to the Department of Pathology for histopathological examination.

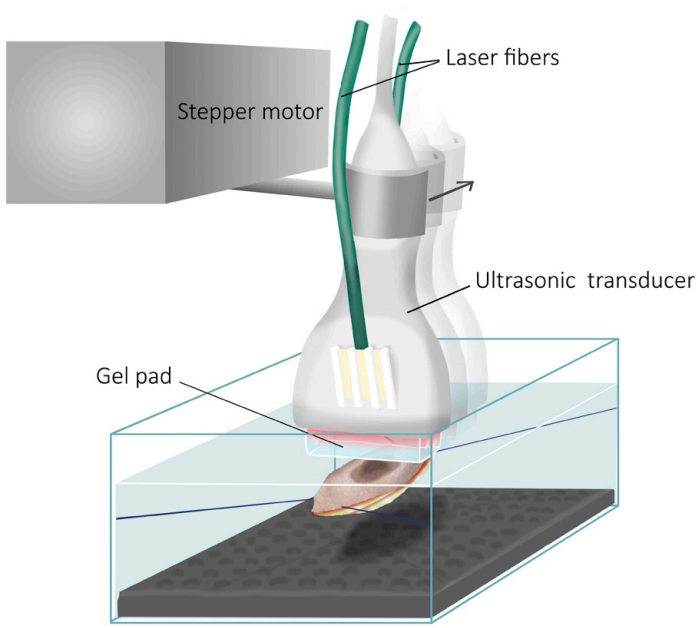

Figure 10. PAI experimental setup.
The stepper motor moves the PA transducer along the *ex vivo* lesion. A gel pad is used to simulate an *in vivo* setup, in which there must be a distance between the laser and the skin surface. (Illustration by the author.)

Photoacoustic imaging equipment

A Vevo LAZR-X (FUJIFILM VisualSonics Inc., Toronto, ON, Canada) hybrid imaging system was used in the first three studies. This system combines PAI with linear array high-frequency ultrasound. The use of a linear array transducer generates both PA and high-frequency ultrasound images, which can then be fused. In this system, fiber optic bundles coupled to a 20-Hz tunable laser with a nanosecond pulse duration are inserted on each side of the ultrasonic transducer, illuminating the skin surface with two planar light beams. The laser can be used in two wavelength ranges; 680-970 nm and 1200-2000 nm. However, due to intense water absorption in the longer wavelength range, only the shorter wavelength range was used in this work. To obtain detailed spectral information from the tumors, 59 excitation wavelengths were used in 5 nm steps (680, 685, 690 nm, etc.). Prior to the measurements, the pulse fluence (optical power per unit area) was calibrated for each wavelength so that the signal could be corrected for wavelength-dependent fluence variations. In the first study, a 40 MHz ultrasound transducer (MX400, VisualSonics Inc.) with a center frequency of 30 MHz and a bandwidth of 22-40 MHz was used to detect the acoustic waves generated by illuminating the tissue. This transducer has a measuring depth of 20 mm and provides an axial resolution of 50 µm and a lateral resolution of 110 µm. Its imaging width is 13 mm. In the second and third studies, a second transducer (MX250, VisualSonics Inc.) was also used to examine tumors ≥13 mm wide. This transducer has a center frequency of 20 MHz and a bandwidth of 13-24 MHz. Its axial resolution is 75 µm and its lateral resolution is 165 µm. To enable 3D imaging, limit motion artefacts, and control the illumination angle, the laser-coupled transducer was mounted on an adjustable arm with a stepper motor (Mounting Accessory, GCX Corporation, Petaluma, CA, USA), which moved the transducer in 0.5 mm steps along the tumor (Figure 10). The resulting 2D images could then be aligned and compiled to form one 3D image. With the above settings, the acquisition time was ~6½ minutes per cm along the y-axis of the lesion.

Hyperspectral imaging equipment

A custom-built hyperspectral camera from the HySpex model series (Norsk Elektro Optikk, Oslo, Norway) was used in the fourth study (Paper IV). A tungsten-halogen lamp with a peak temperature of 2900 K was used to illuminate the tumors with broad-spectrum white light. The camera has a spectral sensitivity from 600-1700 nm, i.e. from the visual and far into the infrared range. This spectral bandwidth is split into 322 spectral bands, which gives a spectral resolution of approximately 3.5 nm. Spectra were recorded from continuous points along a 32 mm thin line on the surface of the lesion. Each line has a spatial resolution of 50 µm (640 pixels). Hence, every scanned line produces 182,000

(640x322) spectral data points in a single aquisition. The tumors were scanned line by line, covering the whole surface of the lesions, thereby generating a vast amount of data. These lines were then stitched together to form a complete hyperspectral image. To normalize the spectrum, a white reference (Spectralon®, WS1, Ocean Optics) reflecting 50% of incoming light at all wavelengths was placed next to the lesion and imaged together with the lesion (Figure 11). A dark reference was also obtained by turning the light source off and repeating the measurements. The dark reference was used to account for background or electronic noise. The HSI acquisition time was up to 18 seconds per cm.

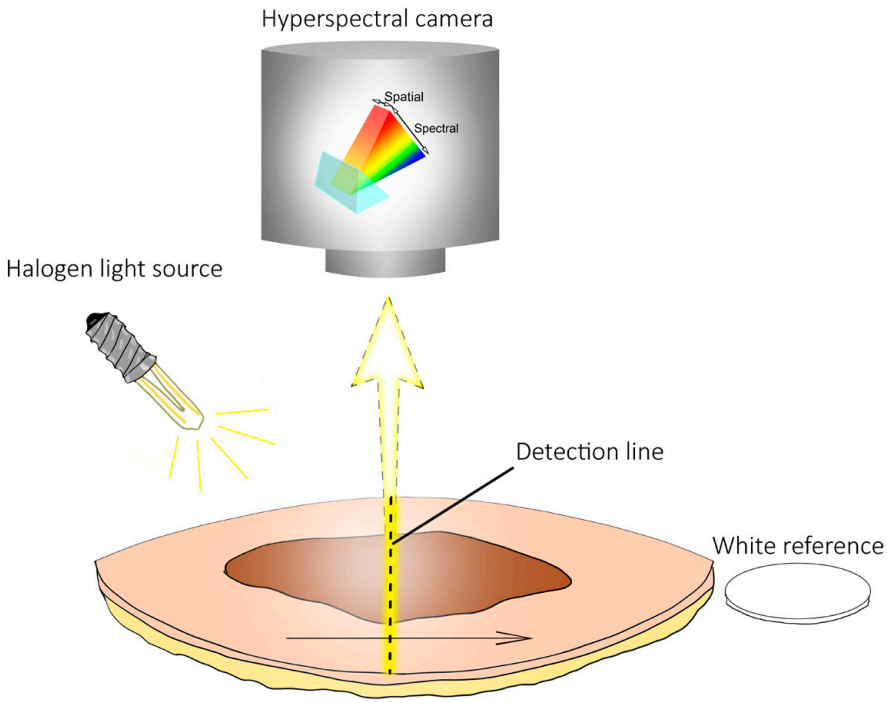

Figure 11. HSI experimental setup.
A white light is used to illuminate the lesion surface. A line is thereafter imaged onto an area detector. Prior to reaching the detector, the light is dispersed by a prism at each point along the line such that one dimension of the detector area captures the spectral information, while the other dimension captures the spatial information. A hyperspectral image is obtained by scanning the lesion line by line across the surface. A white reference is also scanned for each lesion. (Illustration by the author.)

Imaging of skin tumors

The variable and unpredictable molecular compositions of human tissue makes imaging from spectral data a complex process, and hence, there is no standard technique for spectral analysis of the skin. Throughout this research, different techniques for spectral unmixing were tested and developed, from linear spectral unmixing (Papers I-II) to a statistical detection method (AMF) (Paper III), and machine learning (Paper IV).

Photoacoustic imaging of cSCCs using linear spectral unmixing

Measurements were carried out *ex vivo* on 33 cSCCs to determine whether the mean tumor spectra (as a function of wavelength) could be used for imaging (Paper I). All the PA scans were processed using VisualSonics Vevo LAB 3.1.0 software. Regions of interest were defined in the ultrasound images by hand. To obtain reference spectra from the cSCCs and healthy tissue, freehand regions of interest were drawn in the (apparent) center of the cSCC and in seemingly healthy tissue at the wedge-shaped edges of the excised lesions, respectively. After establishing that there was a significant difference between the mean signal from all cSCCs and the mean signal from all healthy tissue, these mean spectra (as a function of wavelength) were used in a linear spectral unmixing algorithm to map the distribution of cSCC-resembling spectra. Linear spectral unmixing was also used to map hemoglobin content, using known spectra for deoxygenated and oxygenated hemoglobin. The anatomical location of cSCC-resembling spectra and hemoglobin was visualized by overlaying the unmixed PA images on a 3D ultrasound image.

Photoacoustic imaging of melanomas and nevi using linear spectral unmixing

In the next study, individual spectra were recorded *ex vivo* of 52 suspected malignant melanomas using PAI (Paper II). The reference spectra from regions of tumor and healthy tissue were obtained using an absorption profile from the whole excised lesion, taking advantage of the high absorption of melanin in the tumors. An algorithm was then developed for use in linear spectral unmixing, which classified pixels as belonging to tumor or healthy tissue. In short, the method was as follows. Raw data from the VisualSonics Vevo LAB 3.1.0 software were imported into MATLAB R2017b (MathWorks Inc., Natick, MA, USA) where ultrasound images were used to automatically remove unwanted signals from the ultrasound gel, protective plastic, and the saline solution, using an intensity histogram. A heat map showing the change in the wavelength-dependent absorption across the entire lesion was then generated. With the presumption that

an increase in melanin is indicative of melanoma, the overall PA intensity (averaged across all wavelengths), was used to identify the location along the sample most likely representing tumor (highest intensity) and healthy tissue (lowest intensity). The cross-sectional PA images from these two locations were then used to extract reference spectra representing tumor and healthy tissue. Using the ultrasound image as a guide, a spatial average of the intensity at each wavelength was obtained over an area of the tumor or healthy tissue, spanning across the epidermis and dermis. The two resulting spectra were then used as so-called endmember spectra ($\boldsymbol{S}_i$) in the linear spectral unmixing equation below to classify each pixel:

$$\boldsymbol{M} = \sum_{i=1}^{N} a_i \boldsymbol{S}_i + \boldsymbol{w} \tag{1}$$

where $\boldsymbol{M}$ is a vector representing the measured PA spectrum in a single pixel, a_i are the linear coefficients (fractional abundances) of each endmember (known chromophore or defined) spectrum $\boldsymbol{S}_i$, and **w** accounts for spectral noise.

After adding a criterion stating that the sum of the linear coefficients (a_i) must be 1, which essentially creates a scale ranging from $a_i = 0$ (100% healthy tissue) to $a_i = 1$ (100% tumor), an automatic threshold function was applied where any pixel yielding $a_i > 0.5$ was classified as tumorous, and $a_i \leq 0.5$ was classified as healthy. A pixel-by-pixel analysis using this criterion could then not only classify the pixels as tumorous or healthy, but also to what degree their spectra resembled the tumor spectrum. Finally, the pixels classified as tumor were color-coded and overlaid on the corresponding ultrasound image to show their location within the excised lesion.

Photoacoustic imaging of melanomas using AMF

In the third study, the AMF method was investigated for spectral unmixing. AMF is based on statistical detection, as opposed to linear regression in linear spectral unmixing. The method was first tested on a phantom and then on seven malignant melanomas *ex vivo* (included in the study in Paper II). The data were processed in MATLAB. To reduce noise, pixels with an intensity of below 2% of the maximum intensity were removed, and a moving average filter was applied to the pixel spectra to reduce sudden fluctuations. By calculating a detection value for each pixel, AMF determined the similarity of the pixel spectrum to the target spectrum (i.e. a defined tumor spectrum) using the equation below:

$$D(x_r) = \frac{(\mu_t - \mu_b)^{\mathrm{T}} \Sigma^{-1} (x_r - \mu_b)}{(\mu_t - \mu_b)^{\mathrm{T}} \Sigma^{-1} (\mu_t - \mu_b)} \tag{2}$$

where D is the AMF detection value for each pixel at position r in the image, μ_t is the target reference spectrum, μ_b is the mean background spectrum, Σ is the background covariance matrix, T is the matrix transpose operator, and x_r corresponds to the multispectral data at position r. D is a measure of the probability that a spectrum in a pixel belongs to the target. By applying a threshold to D, pixels can be divided into either target or background. The μ_t target spectrum and the μ_b background specta were defined as the mean of the target spectra from the multiwavelength PA images, selected from regions of interest in the top layer of the tumors and healthy tissue. To separate target (tumor) pixels from the background, an algorithm that selected the threshold automatically was computed (for further details please see Section 2.3 in Paper III).

Hyperspectral imaging of various skin tumors using machine learning

In the final study (Paper IV), HSI was used to provide highly detailed spectral information from the surface of suspected BCCs, cSCCs, and malignant melanomas. The spectral output was converted to absorbance by calculating the negative logarithm of the normalized signal, using the following equation:

$$A(\lambda) = -log_{10}\left(I(\lambda)/I_{Ref}(\lambda)\right) \tag{3}$$

where A(λ) is the absorbance (as a function of wavelength), I(λ) is the diffusely reflected spectrum (as a function of wavelength) and $I_{Ref}(\lambda)$ is the white reference.

Three different machine learning networks (ANNs) were used to automatically image and delineate different tumors, irrespective of the final diagnosis of the tumors. To train the ANNs, pixels were selected and classified as tumor or healthy. This selection was guided by HSI overview photos that could be related to histopathological cut-out templates and fixed tissue sections. The pixels classified as tumor were usually chosen from the center of the tumors, and those classified as healthy were chosen from the wedge-shaped edges of the lesions. The 3 different ANNs were: 1) a multi-layer perceptron (MLP), 2) an additional multi-layer perceptron trained on multivariate curve-resolution-alternating least-squares (MLP with MCR-ALS), and 3) a 1D convolutional neural network (1D CNN).

MCR-ALS analysis was used to extract the most common spectral features from all tumors combined, with the spectral components representing particular compositions of the tissue. As the signal-to-noise ratio was very low in the spectral range 1400-1600 nm, this spectral range was excluded from the analysis with MCR-ALS. The MLP and 1D CNN were trained on raw spectral features, and the MLP with MCR-ALS was trained on the 8 MCR-ALS extracted components. MLP and 1D CNN both consider 1 pixel at a time as input, but the CNN also weighs in neighboring spectral features.

After training, the ANNs were used to make predictions about the probability that each pixel represented tumor, generating prediction maps. A segmentation algorithm was then used to delineate the tumors. In this algorithm, a function acting as a "sandpile" was used to add spatial context to the pixels and thereby reduce areas of misclassified pixels. This resulted in larger sandpiles in the center of the tumors and smaller sandpiles piles in areas where pixels had been misclassified due, for example, to hair, marker pen ink, or noise. An active contour algorithm (156) was then used to define the tumor edges. The active contour algorithm behaves like a rope, tightening around the sandpiles where it passes small noise hills until it reaches an equilibrium.

Finally, the saliency was calculated to assess the impact of different spectral ranges on pixel classification. Saliency is a measure of how the output changes when input features are disturbed. Greater changes in output indicate higher importance of the input and show a higher saliency. Based on observations of saliency peaks, the ANNs were again trained on selected spectral ranges (600-750 nm, 1000-1200 nm, and 1300-1400 nm), generating new tumor images that were delineated to illustrate how tumor dimensions changed depending on the spectral range.

Statistical analysis

All calculations and statistical analysis were performed in MATLAB. Significance was defined as $p < 0.05$. A Pearson correlation coefficient (r) > 0.7 was considered to indicate a strong correlation.

Comparison of tumor and healthy spectra

The mean paired difference in PA absorption spectra between cSCCs and surrounding healthy skin was analyzed using the two-way paired t-test for repeated measures (Paper I). The absorption spectra from melanomas, nevi, and healthy tissue were analyzed using the two-way ANOVA test, and Grubb's test was used to identify outliers (Paper II).

Comparison of imaging measurements with histopathological measurements

The correlation between tumor width and thickness measured with PAI and histopathological examination was determined using the Pearson correlation coefficient (Papers II and IV) and the relative mean squared error (Paper IV). Bland–Altman plots were used to demonstrate differences between the measurements in the third study (Paper III).

Results and discussion

Our group has previously reported the potential of PAI to image human BCCs (110). The feasibility of using PAI for imaging and delineation of human cSCCs, melanoma, and nevi was explored in the present research. A requirement for successful imaging of a skin tumor using spectral techniques is that the spectral signal of the tumor differs sufficiently from the spectral signal of the surrounding healthy skin. This was investigated in the first two studies, where the mean spectral signals from cSCCs, malignant melanomas, and nevi were compared to the mean spectral signals from healthy skin. Spectral unmixing algorithms were then applied to locate and image the tumors, and the correlation between the results of imaging methods and histopathological examination was determined in the second and third study. In the fourth study, machine learning was used on HSI data of different tumor types. The ANNs were trained on individual tumor spectra, assuming a spectral difference between tumor and healthy tissue. The ANNs were then used to predict and delineate the tumors, and correlations to histopathological measurements were determined to evaluate the performance of the method.

Photoacoustic imaging of cSCCs

The results from the first study showed that there was a significant difference between the mean PA spectral signals from cSCCs and healthy skin in the wavelength range 765-960 nm (Figure 12).

It was then demonstrated that the mean PA tumor spectrum could be used in a linear unmixing algorithm for cSCC imaging in 3D (Figure 13).

The molecular composition of the tumors was not investigated. Keratin, which is probably the most abundant chromophore in cSCC, absorbs light mainly in the ultravioulet region (157), and its contribution to the tumor signal can thus be assumed to be negligible. Only a few studies have been performed previously on human cSCCs using PAI in which the melanin and hemoglobin signals were used to provide contrast, but none investigated using the cSCC signal for imaging. In the first PA study including human NMSCs, Zeitouni et al. (108) demonstrated in one BCC and one cSCC that PA could be used as a supplement to high-frequency ultrasound to improve tumor demarcation *in vivo* using one wavelength (580 nm) to image hemoglobin absorption. Later, Attia et al. (107) performed multispectral

PA scanning of 21 suspected NMSCs (number of cSCCs unknown) *in vivo*, using melanin and hemoglobin for imaging. Their study showed good correlation with histopathological measurements when using a 3D ultrasonic transducer. In another study, the same research group used multispectral PAI to study 19 BCCs and 6 cSCCs *in vivo* (106), again using the hemoglobin and melanin signals for imaging. The measured tumor dimensions correlated well with the results of histopathology. However, it was reported that the PA measurements were less accurate at shallow tumor depths. This was attributed to anisotropic resolution in the peripheral regions of the field of view.

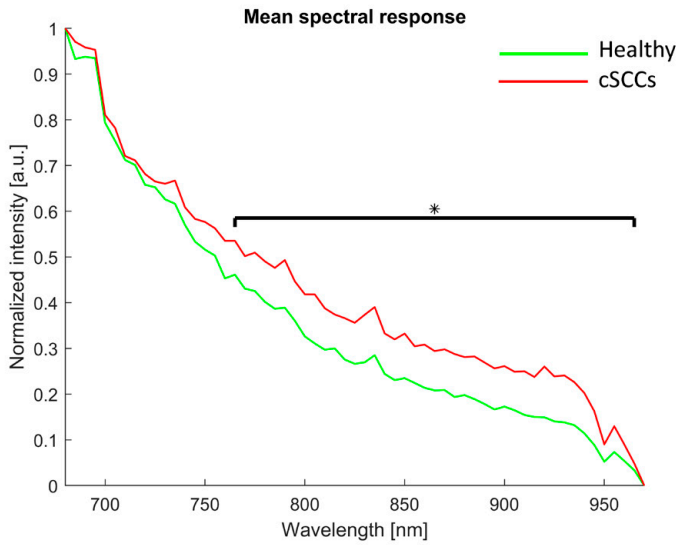

Figure 12. The mean PA spectral response of cSCCs and surrounding healthy skin.
The figure shows *ex vivo* measurements from 33 tumors, A significant difference (*) was seen between the spectral signatures for wavelengths in the range 765-960 nm ($p < .05$).

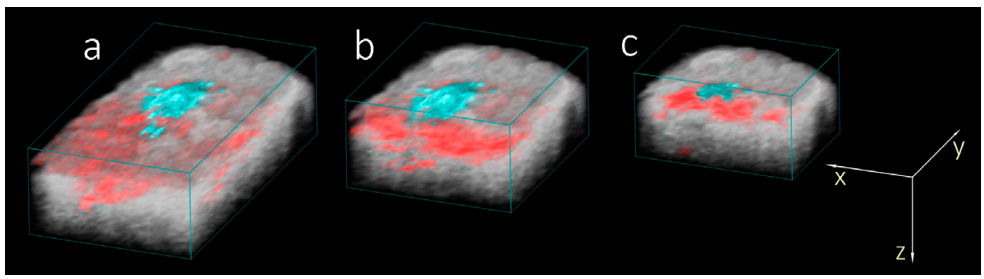

Figure 13. PAI of a cSCC.
Representative example of a PA image of a cSCC (a), and two slices of the lesion along the y-axis to reveal the depth of the tumor (b and c). The mean spectrum from all cSCCs was used to map the cSCC (turquoise). Previously known spectra for deoxygenated and oxygenated hemoglobin were used to map the distribution of hemoglobin (red).

A major limitation of the study is that the cSCCs were imaged *ex vivo*. However, the multispectral 3D measurements made *in vivo* were severely impaired by motion artifacts. Even if the patients were perfectly still, motion artifacts could still be caused by breathing or heartbeats. The motion artifacts could probably have been reduced by tuning the PA settings, for example, by reducing the number of excitation wavelengths, or increasing the distance between the 2D acquisitions. However, this would reduce the quality of the spectral signal and make tumor delineation less precise. *In vivo* imaging may be possible in the future by developing and applying a motion tracking algorithm to the PA images (158, 159).

Although it was demonstrated that the mean tumor signal could be used for imaging, skin tumors of the same type exhibit considerable morphological and molecular variation. It was therefore deemed that using individual spectra in the spectral analysis would probably be a better approach for tumor imaging, and this approach was used in the subsequent studies.

Photoacoustic imaging of melanomas and nevi

In the second study, it was first shown that there was a significant difference between the PA tumor spectrum for melanomas and nevi, compared to healthy tissue (Figure 14).

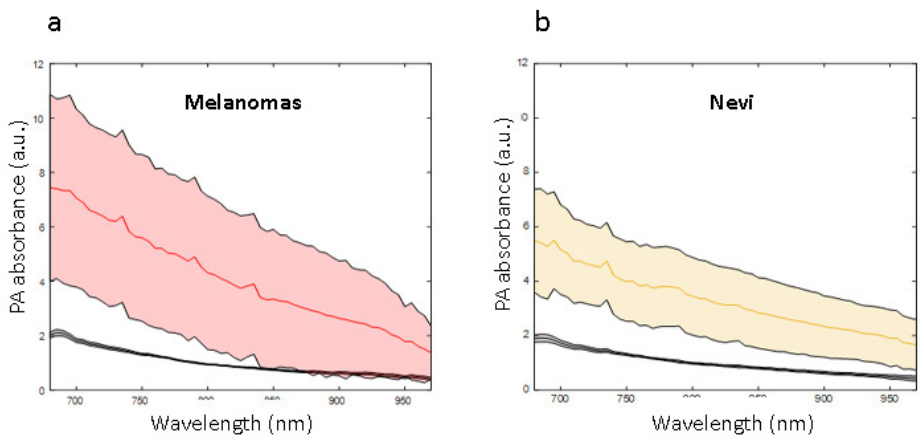

Figure 14. Mean PA absorption spectra from melanomas and nevi.
PA absorption spectra obtained from (a) 25 melanomas (left) and (b) 26 nevi (right), compared to the surrounding healthy tissue (black line). Data are shown as mean ±1 SD. Statistical analysis was performed using two-way ANOVA and Grubb's test was performed to identify outliers. One outlier was identified and removed from the nevi group. A clear difference can be seen between the spectral signatures from healthy tissue and melanomas ($p<0.001$), and between healthy tissue and nevi ($p<0.0001$).

An algorithm was developed to automatically identify regions from which reference tumor spectra and healthy spectra could be extracted. An automatic threshold algorithm was also developed for the identification of tumor pixels in linear spectral unmixing. The results showed that individual tumor spectra could be used to image melanomas and nevi in 3D, using these automatic algorithms (Figure 15).

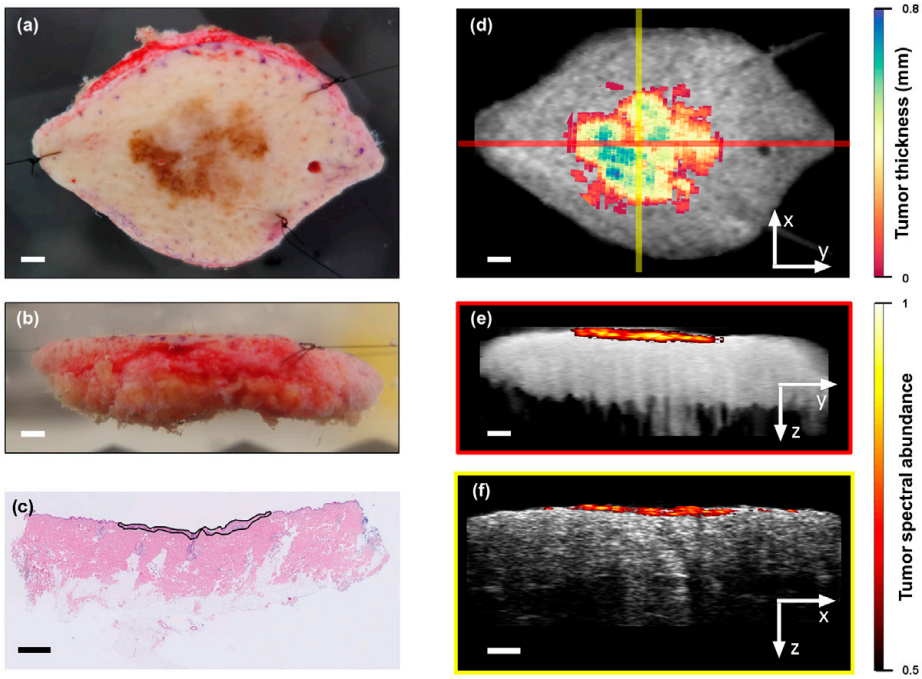

Figure 15. PAI of a melanoma *in situ* in 3D.
(a) and (d) show longitudinal sections from above, while (b) and (e) and (c) and (f) show cross sections. The left column, (a) and (b) shows photographs, and the histopathological image (c). The right column (d-f) shows PA images after linear spectral unmixing with an automatic threshold for tumor pixel identification. The information obtained from PAI is indicated by the colored pixels superimposed on the grayscale ultrasound images. Scale bars represent 2 mm.

After imaging the melanomas and nevi, the PA-measured tumor widths and thickness were compared to histopathological measurements. The results showed a strong correlation for melanoma width; a moderate correlation for nevi width and a strong correlation for both melanomas and nevi for the thickness (Figure 16).

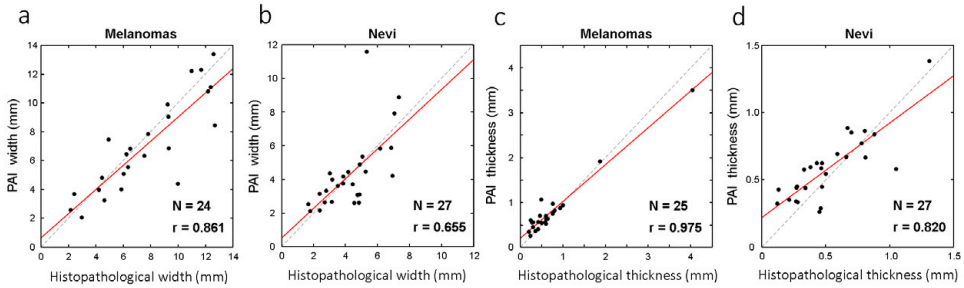

Figure 16. Comparison of PAI with linear spectral unmixing and histopathological examination in determining tumor width and thickness

Scatter plots showing the correlation between PAI and histopathological measurements of tumor widths (a-b) and thicknesses (c-d). The Pearson correlation coefficients (r) indicate a strong correlation for melanoma width and thickness, as well as nevi thickness, and a moderate correlation for nevi width.

The results showed that for width measurements, the number of overestimations and underestimations with PAI were almost equal. In thin melanomas and nevi (≤ 1.0 mm), PAI tended to overestimate the thickness slightly. In thick melanomas and nevi (> 1.0 mm), PAI underestimated the thickness slightly.

A different method for spectral analysis, AMF, was then investigated, and an automatic threshold selection algorithm (ATS) developed for the differentiation between tumor and healthy tissue pixels. The AMF-ATS algorithm was first tested on a phantom and then on 7 of the melanomas imaged with PAI. The results showed that while AMF alone could not delineate the melanomas clearly, applying the automatic threshold algorithm made delineation possible (Figure 17).

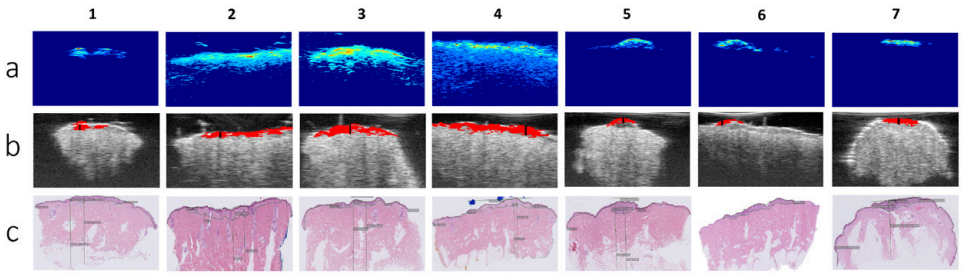

Figure 17. Comparison of AMF detection results in seven malignant melanomas, examined *ex vivo*, with and without ATS.

(a) The results using AMF only, and (b) the results after applying ATS, overlaid on the ultrasound images. Pixels classified as tumor are shown in red. (c) Histopathological sections.

The width and thickness of the melanomas obtained with PAI (AMF-ATS) were then compared to those obtained by histopathology (Figure 18).

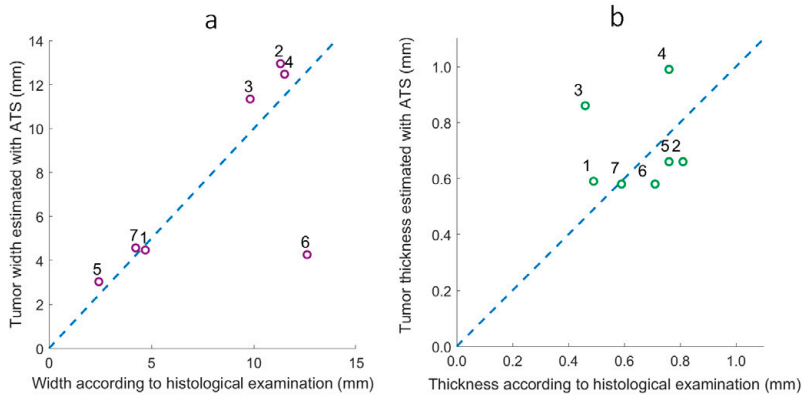

Figure 18. Comparison of PAI with AMF-ATS and histopathological examination in determining tumor width and thickness.
Scatter plots showing the PAI width (a) and thickness (b) of seven melanomas using the AMF-ATS algorithm versus the width and thickness determined by histological examination.

The results presented in Papers II and III show the ability of PAI to map melanomas and nevi in 3D using individual tumor spectra. Only a few studies have previously studied PAI of human melanomas, and the spectral information used in those studies was more limited than that presented in this dissertation. Zhou et al. (112) used PAI with one excitation wavelength (680 nm) for 2D *in vivo* imaging of melanin in 10 melanomas. In their study, melanomas with thicknesses up to 6.0 mm were successfully imaged, and the thickness correlated well with the histopathological thickness. Three-dimensional imaging of melanomas and nevi using several wavelengths, and correlation to histopathology, have been reported by Park et al. (111) and Breathnach et al. (97). Park et al. scanned 6 melanomas *in vivo* using PAI with five excitation wavelengths (700, 756, 796, 866, and 900 nm). The melanin absorption spectrum was used to visualize the tumors, and measurements of the tumors correlated well with histopathology (111). In their study, a nodular melanoma with a PA depth of 9.1 mm and a histopathological depth of 8.0 mm was visualized, which is the thickest melanoma measured with PAI to date. One problem associated with using only the melanin spectrum for melanoma imaging is that not only mutated melanocytes, but also normal melanocytes, keratinocytes, and melanophages (a type of macrophage) contain melanin, which could lead to overestimation of the tumor dimensions. Amelanotic melanomas with little or no melanin would be difficult to image, and imaging melanomas thicker than 2.0 mm could be problematic as thicker melanomas may have a significantly lower melanin content than thinner melanomas (160). Breathnach et al. (97) used PAI to scan 32 pigmented tumors (including 6 melanomas) *in vivo* using 30 excitation wavelengths from 680

to 970 nm in the most pigmented part of the lesion. Five excitation wavelengths were then used for multiwavelength 3D scans of the entire lesion, and unmixing was performed to image regions of absorption that matched the spectrum of the most pigmented part. The PA tumor thickness was strongly correlated to histopathological findings ($r \geq 0.98$).

The results presented in Papers II and III showed that thickness measurements of melanomas and nevi made with PAI were well correlated with histopathological findings, which is in line with the results of the previous studies described above. However, the PA-measured tumor widths were not as well correlated with histopathological measurements as the thickness. The larger inconsistency in width could have several causes, for example relating to the histopathological sectioning, variations in shrinkage of the lesions when placed in formalin etc. Another reason could be the higher concentration of melanin in the epidermis of healthy skin, which could cause the healthy skin spectrum to look more like tumor in the epidermis, compared to the dermis. The results regarding the correlation for tumor thickness in these papers should be interpreted with caution as most of the tumors in these studies were thin (<1.0 mm). Small differences in thickness between the two methods can be expected as the histopathological sections may not correspond exactly with the cross-sectional PA image. The relative difference resulting from this misalignment will naturally be greater in thin tumors than in thick tumors. The thickest melanoma had a histopathological thickness of 4.04 mm and a PAI-measured thickness of 3.5 mm, meaning that PAI slightly underestimated the thickness. This underestimation is probably the result of light fluence attenuation. The light fluence is attenuated with tissue depth, leading to darker areas with poorer contrast deeper in the skin. Mouse models have been used in many preclinical studies to investigate the spatial resolution achievable with PAI (91, 161, 162). The PA devices used in those studies provide almost uniform illumination throughout the whole body of the mouse, with signal detection in almost all directions, enabling high spatial resolution (163). However, it is not possible to illuminate most anatomical areas in humans from all directions, which increases the effect of fluence attenuation and reduces the resolution. Other factors that affect the PAI resolution are readout noise, laser power fluctuations and imaging artifacts such as motion.

The PA pulse fluence was calibrated at every excitation wavelength before imaging. However, as every excitation wavelength will be absorbed differently through all layers of the skin (due to the composition of endogenous chromophores), the residual fluence at every wavelength will be different. This phenomenon increases with depth and is known as spectral coloring. The effects of spectral coloring were not known or compensated for in the work presented in this dissertation, and PA spectra and measurements of deeper tumors should therefore be interpreted with caution. A good correlation was found between the PAI-measured thickness of the melanomas and nevi, and the histopathological measurements, which may be due to the fact that most tumors were ≤1.0 mm

thick. The amount of light delivered to a specific region of the skin can be estimated using Monte Carlo simulations (164). However, such simulations are difficult because they require models that simulate different skin tumors and variations in healthy skin both intra- and inter-individually.

Automatic algorithms were developed for tumor pixel identification and tumor border delineation, and it was shown that the algorithms could improve the imaging of melanomas and nevi. Breathnach et al. (97) suggested that single-wavelength images could provide similar contrast between tumor and healthy tissue to spectral unmixing of multispectral images. However, the results of unmixing single-wavelength PA images would depend on the intensity threshold set by the user, while automatic algorithms for thresholding offer a more objective approach to PAI.

Hyperspectral imaging and machine learning for delineation of superficial tumor borders

The results of the studies described above showed that for a few tumors, the PA-measured tumor width was not well correlated with histopathological findings, indicating that it may be difficult to identify the lateral extent of some tumors within the epidermis. Three ANNs were therefore applied to HSI data to delineate the superficial tumor borders of 18 different skin tumors suspected of malignancy (Paper IV). Figure 19 shows an example of HSI spectra extracted from 4 different regions of a melanoma, visualizing the difference in absorbance between the tumor spectrum and the spectrum in seemingly healthy skin.

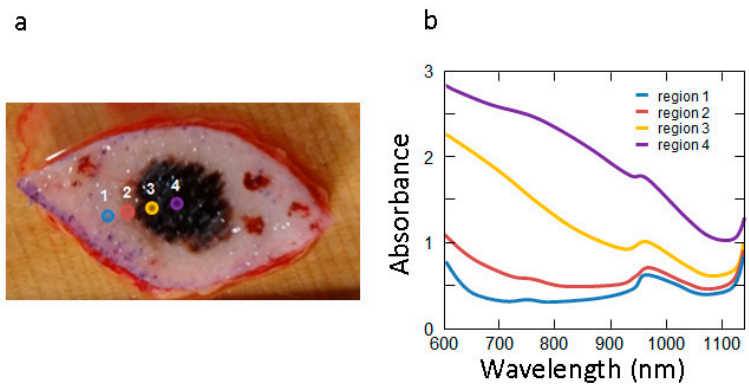

Figure 19. HSI spectra from different regions of a melanoma.
Color photo of a melanoma (a) with colored dots from which absorbance spectra in (b) were obtained with HSI. The figure serves as example of how absorbance can differ between the center of a tumor (region 4, purple) and the seemingly healthy skin outside the tumor (region 1, blue).

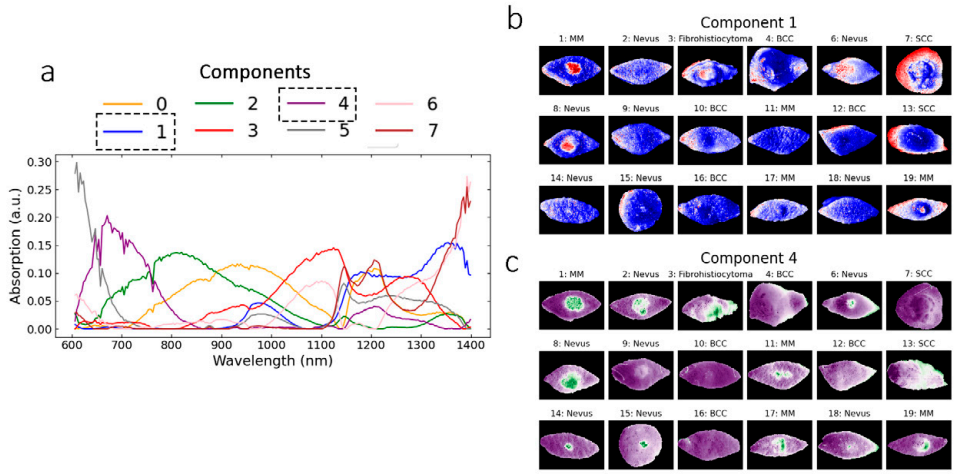

Figure 20. Results of MCR-ALS analysis.
(a) The eight components extracted from all tumor spectra using MCR-ALS. (b and c) Examples of 2 of the 8 spectral component maps (component number 1 and 4 from (a)), showing their contributions in tumor mapping of all 18 tumors. Note that the tumors will be imaged differently depending on the contributions of the components.

MCR-ALS analysis was used to extract the 8 most common spectral features (referred to below as components) from all the tumors combined. The resulting spectral components and examples of their relative contributions to the tumor images are shown in Figure 20.

To classify pixels into tumorous or healthy, the first ANN (MLP with MCR-ALS) was trained on the 8 spectral components. The other two ANNs (MLP and 1-D CNN) were trained on raw spectral features from the tumors and healthy tissue. After training, the ANNs could make predictions about the probability of tumor in each pixel of the excised lesions. A prediction map for all tumors generated by one of the ANNs (MLP with MCR-ALS) is shown in Figure 21, as well as the results for one BCC, generated by all the ANNs.

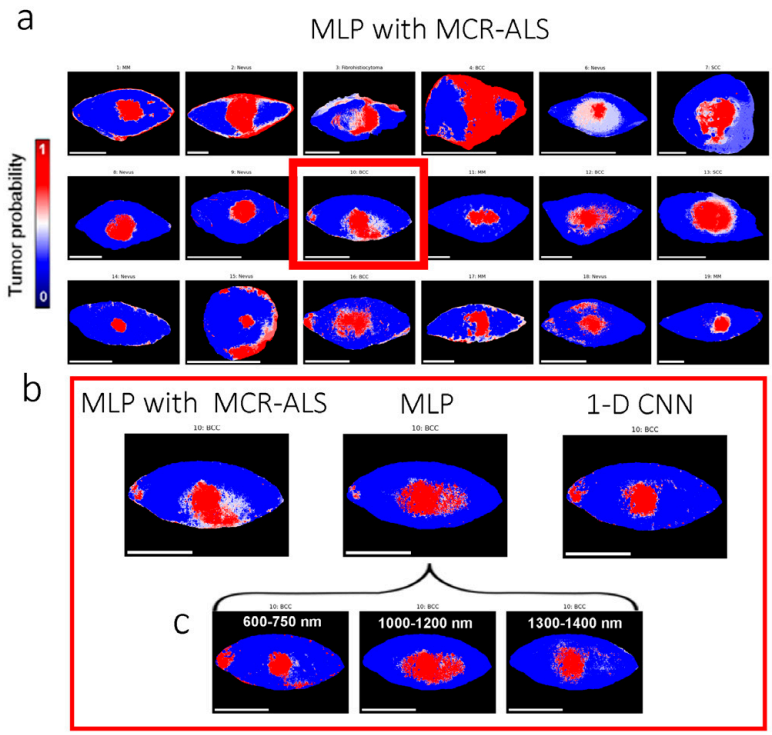

Figure 21. Prediction maps generated by the ANNs.
(a) Prediction maps for the 18 tumors generated by one of the ANNs (MLP with MCR-ALS). The prediction maps show tumor probability, where red represents 100% probability and blue represents 0% probability. The scale bars represent 10 mm (b) Prediction maps for one BCC generated by the three different ANNs. (c) The MLP network was also trained on three spectral ranges based on so-called saliency peaks. Note that the prediction map for the same BCC in (b) and (c) changes depending on the network and spectral range used.

As can be seen in Figure 21 (a), the prediction maps could not clearly identify the tumor borders due to noise. To reduce the influence of noise and delineate the tumors, a segmentation algorithm was used, in which a sandpile function added spatial information to the pixels. The resulting sandpile landscape was then used in an active contour algorithm for all ANNs and tumors, resulting in a delineation of the superficial tumor borders (Figure 22).

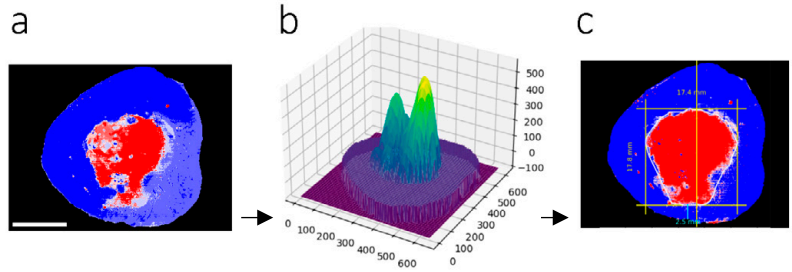

Figure 22. Representative example of delineation of a tumor.
(a) Prediction map of a cSCC generated with one of the ANNs (the MLP with MCR-ALS). (b) A sandpile landscape added to the prediction map, reducing areas with misclassified pixels. (c) Result of applying an active contour algorithm to the sandpile landscape, showing a delineation of the cSCC (white line). The scale bar represents 10 mm.

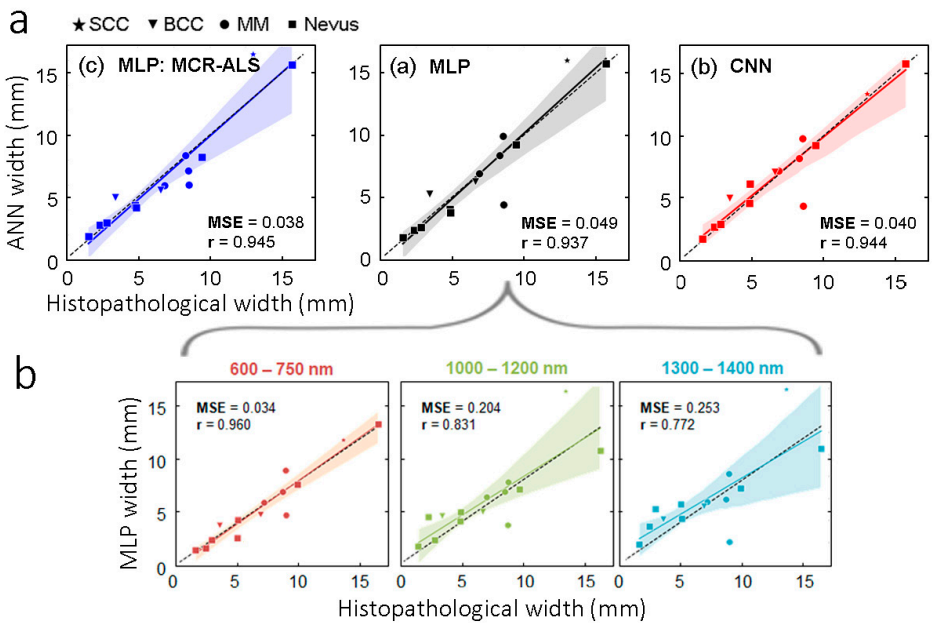

Figure 23. Comparison between tumor widths obtained with the three ANNs and those determined histopathologically
(a) Tumor width correlation with histopathology using the three ANNs (MLP with MCR-ALS, MLP and 1-D CNN), with all networks showing strong correlations. (b) The correlation changed when the MLP network was trained on different spectral ranges. The Pearson correlation coefficient (r) is represented by the solid lines.

After delineation, the tumor widths could be measured and correlated to histopathological measurements. As can be seen in Figure 23, the width was strongly correlated to the histopathological measurements, but the strength of the correlation differed slightly depending on which ANN was used. The MLP with MCR-ALS gave the strongest correlation. Figure 23 also shows that the predicted tumor width changed when the ANNs were trained on different spectral ranges.

The results presented in Paper IV show how machine learning in the form of ANNs can be applied to HSI data to automatically predict tumor probability at the skin surface, and how segmentation algorithms then can delineate the tumors. Previous studies on machine learning for tumor delineation have generally relied on spatial information in the form of manually defined tumor borders to train the models. In this work, by training the models on spectra, the models did not need spatial information for training. There are few previous studies on skin tumor delineation using HSI, but these include HSI delineation of lentigo maligna (138), ill-defined BCCs (139), and field-cancerized skin (140). In one of these studies, Salmivuori et al. (139) used HSI and linear unmixing to delineate 16 ill-defined BCCs. In 12 of the 16 cases, HSI delineated the BCCs more accurately than the naked eye and dermatoscopy. Although the results of the present study showed a strong correlation with histopathologically measured widths, a limitation of this study is that the tumor widths were not compared to those obtained with the naked eye or dermatoscopy.

All the prediction maps generated by the ANNs contained noise, and in four of the tumors, the noise was so large that the tumors could not be delineated. The reason for the noise is unclear, but some may originate from the interaction of light with tissue below the surface, or artefacts such as hair, blood, ink, or exposed subcutaneous fat under the incision. None of these artifacts, apart from hair, would be present in future *in vivo* studies with HSI.

The correlation plots in Paper IV demonstrate how the predicted tumor widths differed depending on the type of ANN and the spectral range used for training the model. This is probably due to several factors. For example, the molecular composition changes across the tumors in an unpredictable way, which complicates training, especially if the training pixels are chosen from small regions of the tumor and healthy tissue, which was the case in this study. Other factors affecting training could be signal-disturbing artifacts, or the fact that individual tumor spectra were used for training. The predictions might have been more robust if the ANNs had been trained on larger datasets with specific tumor types.

The advantage of using individual tumor spectra for training is that no ground truth segmentation masks are needed to identify tumor borders. In addition to the disadvantage of using a subjective method of training the ANNs, large datasets with ground truth segmentation of skin tumors by experts are lacking (145). The method described in Paper IV circumvents the need for ground truth images but would benefit from training on histopathological sections if the locations of these were matched accurately to corresponding sections of the HSI images.

Skin types

Most of the tumors studied were in patients with Fitzpatrick skin type II (e.g. fair skin). The contrast between light skin, with little melanin, and pigmented tumors makes the differentiation of spectral signals easier than in individuals with darker skin. It is therefore not clear whether the results of these studies could be applied to an international population with a greater range of skin types.

Differential diagnosis

No attempts were made to use these imaging techniques as a diagnostic tool to discriminate between benign and malignant tumors, or to differentiate between malignant tumors of different types. This would require larger studies, due to the large variation in phenotypes of different tumors.

Conclusions and future perspectives

The results presented in this dissertation demonstrate the feasibility of using spectral techniques such as PAI and hyperspectral imaging for skin tumor delineation *ex vivo*. Other non-invasive techniques for skin tumor imaging are limited by factors such as resolution, molecular contrast and penetration depth. Both PAI and HSI provide high resolution with molecular contrast, and in addition, PAI can image tissue deeper than previously possible with other optical techniques. Due to the novelty of these techniques for tissue imaging, few previous studies have been performed on skin tumors, and those that have varied with regard to equipment, settings, and method of spectral analysis. It has been demonstrated in this work that PAI and HSI at multiple wavelengths can detect differences between tumor and healthy tissue, which can be used to image and delineate tumors in 2D (HSI) and 3D (PAI).

It has also been demonstrated that algorithms and machine learning can be developed and applied to the spectral image data, which could potentially circumvent the need for subjective assessments by medical experts. If spectral techniques could be used preoperatively to guide surgery, this could reduce the risk of non-radical excision or excessive removal of healthy skin in sensitive areas such as the eyelids or face. These imaging techniques could also replace histological examination during Mohs micrographic surgery, allowing unfixed tissue to be examined intraoperatively. However, further development and *in vivo* studies including patients with a wide range of skin types, as well as standardization of the methods, are required to make the techniques suitable for clinical use.

Acknowledgements

This work would not have been possible without the help, drive, and positive spirit of many people I have worked with and encountered along the way. I would especially like to thank:

Malin Malmsjö, professor and my main supervisor. Your world is full of opportunities, and no problem is insurmountable. You see the potential in everyone around you and have helped me understand the value of collaboration. Thank you for always being available, and for your invaluable guidance, support, and trust.

All the staff at the Department of Dermatology, for believing in the project and providing the basis for patient-centered research in these studies. Special thanks to **Dr. Bertil Persson,** for his invaluable help and advice.

Aboma Merdasa, my co-supervisor, and research engineer specialized in spectroscopy. I wish everyone could have such a positive and encouraging colleague. Your never-ending enthusiasm and interest in the projects are infectious. Thanks for your endurance during our late-night Teams sessions with students, for bringing the research group together at social events, for keeping our energy levels high with healthy snacks, and for always being so generous with your help.

Bodil Gesslein, my co-supervisor. Your unusually clear common sense and professionalism is inspiring. Thank you for your advice about scientific writing, your help with applications and your patience when deadlines were tight.

Karl Engelsberg, my co-supervisor. Your warm care for patients and colleagues is admirable. Thanks for all your encouragement, and for always lifting my mood a bit higher.

John Albinsson, research engineer, specialized in ultrasound. I really enjoyed talking to you and hearing your insightful reflections, which often aroused my curiosity and gave rise to new research questions.

Azin Khodaverdi, Tobias Erlöv, and Magnus Cinthio, research colleagues at the Faculty of Engineering, Lund, for their support, collaboration, and valuable insights into PAI and spectral unmixing methods.

Emil Andersson, Victor Olariu, and Carl Troein, research colleagues at the group of Computational Science for Health and Environment, for their patience, collaboration and for trying to help me understand machine learning.

Rafi Sheikh, research colleague, for his visionary and rational approach to our joint research projects. Thank you for your support, and especially for your invaluable help with all types of technical equipment.

Ulf Dahlstrand, research colleague, for his humble way of introducing me to PAI and the art of brainstorming.

Ingemar Gustafsson, my clinical supervisor during my residency and now a colleague at the corneal section. Despite your busy schedule, you made great efforts to pave the way for my surgical training, which has allowed me to develop my clinical skills in parallel with my doctoral studies. Your visionary research ideas and your enthusiasm are inspiring. Also, thanks for always answering your phone!

Agnes Pekar-Lukacs, senior consultant in pathology, for her invaluable advice and thorough work in diagnosing and measuring tumors.

Johanna Berggren, Kajsa Tenland, Magdalena Naumovska, Björn Hammar, Cu Ansson, Josefine Bunke, Magne Stridh, and Linn Engqvist, research colleagues, for generous support and guidance.

Karin Wickerström, Benjamin Sjögren, Yousef Hamid, Douglas Larsson, and Ivan Nicolic, medical students, for their enthusiasm, smart questions and for moving the research forward.

Helen Sheppard, nuclear physicist and professional translator, for her unfailing help with scientific writing and her sharp observations and witty comments.

Sten Kjellström, Kristina Johansson, Lena Rung, Joakim Thylefors, Sabina Andersson, Eva Kretz, and Carin Gustavsson, heads of the Dept. of Ophthalmology during my PhD studies. We are lucky to have had managers that understand the importance of research and that make time for it, despite pressuring schedules at the clinic. Thank you for your support.

Päivi Kannisto, associate professor in gynecology, family friend, and my research mentor. Knowing I could always turn to you for guidance and advice was a fantastic comfort.

My family, Theis, Enna, Björk, and Karl-Erik, for your wittiness, love, and patience during my research. Thank you to my mother and father, my sister, and brother, for your never-ending love and support.

References

1. van Loo E, Mosterd K, Krekels GA, Roozeboom MH, Ostertag JU, Dirksen CD, Steijlen PM, Neumann HA, Nelemans PJ, Kelleners-Smeets NW. Surgical excision versus Mohs' micrographic surgery for basal cell carcinoma of the face: A randomised clinical trial with 10 year follow-up. Eur J Cancer. 2014;50(17):3011-20.
2. van Lee CB, Roorda BM, Wakkee M, Voorham Q, Mooyaart AL, de Vijlder HC, Nijsten T, van den Bos RR. Recurrence rates of cutaneous squamous cell carcinoma of the head and neck after Mohs micrographic surgery vs. standard excision: a retrospective cohort study. Br J Dermatol. 2019;181(2):338-43.
3. Thomson J, Hogan S, Leonardi-Bee J, Williams HC, Bath-Hextall FJ. Interventions for basal cell carcinoma of the skin. The Cochrane database of systematic reviews. 2020;11(11):Cd003412.
4. Tolkachjov SN, Brodland DG, Coldiron BM, Fazio MJ, Hruza GJ, Roenigk RK, Rogers HW, Zitelli JA, Winchester DS, Harmon CB. Understanding Mohs Micrographic Surgery: A Review and Practical Guide for the Nondermatologist. Mayo Clin Proc. 2017;92(8):1261-71.
5. Rapini RP. Pitfalls of Mohs micrographic surgery. J Am Acad Dermatol. 1990;22(4):681-6.
6. Yelamos O, Manubens E, Jain M, Chavez-Bourgeois M, Pulijal SV, Dusza SW, Marchetti MA, Barreiro A, Marino ML, Malvehy J, Cordova MA, Rossi AM, Rajadhyaksha M, Halpern AC, Puig S, Marghoob AA, Carrera C. Improvement of diagnostic confidence and management of equivocal skin lesions by integration of reflectance confocal microscopy in daily practice: Prospective study in 2 referral skin cancer centers. J Am Acad Dermatol. 2020;83(4):1057-63.
7. Wang LV, Hu S. Photoacoustic tomography: in vivo imaging from organelles to organs. Science. 2012;335(6075):1458-62.
8. Wassef C, Rao BK. Uses of non-invasive imaging in the diagnosis of skin cancer: an overview of the currently available modalities. Int J Dermatol. 2013;52(12):1481-9.
9. Wortsman X. Ultrasound in dermatology: why, how, and when? Semin Ultrasound CT MR. 2013;34(3):177-95.
10. Khavkin J, Ellis DA. Aging skin: histology, physiology, and pathology. Facial Plast Surg Clin North Am. 2011;19(2):229-34.
11. Andersen KE, Lomholt HB, Thestrup-Pedersen K, Wulf HC. Klinisk dermatologi og venerologi. 3rd ed. Copenhagen: Munksgaard Danmark; 2012. 319 p.
12. D'Orazio J, Jarrett S, Amaro-Ortiz A, Scott T. UV radiation and the skin. Int J Mol Sci. 2013;14(6):12222-48.

13. Agache PG, Agache P, Humbert P, Maibach HI. Measuring the Skin: Springer; 2004.
14. Madan V, Lear JT, Szeimies RM. Non-melanoma skin cancer. Lancet. 2010;375(9715):673-85.
15. Sung H, Ferlay J, Siegel RL, Laversanne M, Soerjomataram I, Jemal A, Bray F. Global Cancer Statistics 2020: GLOBOCAN Estimates of Incidence and Mortality Worldwide for 36 Cancers in 185 Countries. CA Cancer J Clin. 2021;71(3):209-49.
16. Miller SJ. Etiology and pathogenesis of basal cell carcinoma. Clin Dermatol. 1995;13(6):527-36.
17. Peris K, Fargnoli MC, Garbe C, Kaufmann R, Bastholt L, Seguin NB, Bataille V, Marmol VD, Dummer R, Harwood CA, Hauschild A, Holler C, Haedersdal M, Malvehy J, Middleton MR, Morton CA, Nagore E, Stratigos AJ, Szeimies RM, Tagliaferri L, Trakatelli M, Zalaudek I, Eggermont A, Grob JJ, European Dermatology Forum tEAoD-O, the European Organization for R, Treatment of C. Diagnosis and treatment of basal cell carcinoma: European consensus-based interdisciplinary guidelines. Eur J Cancer. 2019;118:10-34.
18. Cancer i siffror 2023: Socialstyrelsen och Cancerfonden; 2023 [updated]. Available from: https://www.socialstyrelsen.se/globalassets/sharepoint-dokument/dokument-webb/statistik/cancer-i-siffror-2023.pdf.
19. Clinical practice guidelines for keratinocyte cancer Sydney: Cancer Council Australia; 2019 [cited 2023 Dec 5]. Available from: https://wiki.cancer.org.au/australiawiki/index.php?oldid=213931.
20. Bath-Hextall FJ, Perkins W, Bong J, Williams HC. Interventions for basal cell carcinoma of the skin. The Cochrane database of systematic reviews. 2007(1):CD003412.
21. Peris K, Fargnoli MC, Kaufmann R, Arenberger P, Bastholt L, Seguin NB, Bataille V, Brochez L, Del Marmol V, Dummer R, Forsea AM, Gaudy-Marqueste C, Harwood CA, Hauschild A, Holler C, Kandolf L, Kellerners-Smeets NWJ, Lallas A, Leiter U, Malvehy J, Marinovic B, Mijuskovic Z, Moreno-Ramirez D, Nagore E, Nathan P, Stratigos AJ, Stockfleth E, Tagliaferri L, Trakatelli M, Vieira R, Zalaudek I, Garbe C, Eado"A EBECUD, Eadv"E. European consensus-based interdisciplinary guideline for diagnosis and treatment of basal cell carcinoma-update 2023. Eur J Cancer. 2023;192:113254.
22. Skivepitelcancer i huden. Nationellt vårdprogram: Regionala cancercentrum i samverkan; 2021 [updated]. Available from: https://kunskapsbanken.cancercentrum.se/globalassets/cancerdiagnoser/hud/skivepitelcancer-i-huden/vardprogram/nationellt-vardprogram-skivepitelcancer-i-huden.pdf.
23. Que SKT, Zwald FO, Schmults CD. Cutaneous squamous cell carcinoma: Incidence, risk factors, diagnosis, and staging. J Am Acad Dermatol. 2018;78(2):237-47.
24. Tan PY, Ek E, Su S, Giorlando F, Dieu T. Incomplete excision of squamous cell carcinoma of the skin: a prospective observational study. Plast Reconstr Surg. 2007;120(4):910-6.
25. Talbot S, Hitchcock B. Incomplete primary excision of cutaneous basal and squamous cell carcinomas in the Bay of Plenty. N Z Med J. 2004;117(1192):U848.

26. Stratigos AJ, Garbe C, Dessinioti C, Lebbe C, van Akkooi A, Bataille V, Bastholt L, Dreno B, Dummer R, Fargnoli MC, Forsea AM, Harwood CA, Hauschild A, Hoeller C, Kandolf-Sekulovic L, Kaufmann R, Kelleners-Smeets NW, Lallas A, Leiter U, Malvehy J, Del Marmol V, Moreno-Ramirez D, Pellacani G, Peris K, Saiag P, Tagliaferri L, Trakatelli M, Ioannides D, Vieira R, Zalaudek I, Arenberger P, Eggermont AMM, Rocken M, Grob JJ, Lorigan P, Eado EEUE, Eortc. European consensus-based interdisciplinary guideline for invasive cutaneous squamous cell carcinoma: Part 2. Treatment-Update 2023. Eur J Cancer. 2023;193:113252.
27. Statistik om nyupptäckta cancerfall 2022: Socialstyrelsen; 2023 [updated 2023-12-19]. Available from: https://www.socialstyrelsen.se/globalassets/sharepoint-dokument/artikelkatalog/statistik/2023-12-8901.pdf.
28. Ugurel S, Rohmel J, Ascierto PA, Becker JC, Flaherty KT, Grob JJ, Hauschild A, Larkin J, Livingstone E, Long GV, Lorigan P, McArthur GA, Ribas A, Robert C, Zimmer L, Schadendorf D, Garbe C. Survival of patients with advanced metastatic melanoma: The impact of MAP kinase pathway inhibition and immune checkpoint inhibition - Update 2019. Eur J Cancer. 2020;130:126-38.
29. Cabrioli C, Maione V, Arisi M, Perantoni M, Guasco Pisani E, Venturini M, Calzavara-Pinton P, Licata G. Surgical margin mapping for lentigo maligna and lentigo maligna melanoma: traditional technique (visual inspection with dermoscopy) versus combined paper tape and reflectance confocal microscopy technique. Int J Dermatol. 2023;62(6):805-11.
30. Nationellt vårdprogram melanom Stockholm: Regionala cancercentrum i samverkan; 2024 [updated 2024-06-11]. Available from: https://kunskapsbanken.cancercentrum.se/diagnoser/melanom/vardprogram/.
31. Keung EZ, Gershenwald JE. The eighth edition American Joint Committee on Cancer (AJCC) melanoma staging system: implications for melanoma treatment and care. Expert Rev Anticancer Ther. 2018;18(8):775-84.
32. Michielin O, van Akkooi ACJ, Ascierto PA, Dummer R, Keilholz U, clinicalguidelines@esmo.org EGCEa. Cutaneous melanoma: ESMO Clinical Practice Guidelines for diagnosis, treatment and follow-updagger. Ann Oncol. 2019;30(12):1884-901.
33. Metze D. Von der Hautbiopsie zur Diagnose. Der Hautarzt. 2007;58(9):735-45.
34. Liersch J, von Kockritz A, Schaller J. Dermatopathology 101: Part 1 - Inflammatory skin diseases. Journal der Deutschen Dermatologischen Gesellschaft = Journal of the German Society of Dermatology : JDDG. 2017;15(1):9-30.
35. Liersch J, von Kockritz A, Schaller J. Dermatopathology 101. Part 2 - Skin tumors. Journal der Deutschen Dermatologischen Gesellschaft = Journal of the German Society of Dermatology : JDDG. 2017;15(9):906-29.
36. Charalambides M, Yannoulias B, Malik N, Mann JK, Celebi P, Veitch D, Wernham A. A review of Mohs micrographic surgery for skin cancer. Part 1: Melanoma and rare skin cancers. Clin Exp Dermatol. 2022;47(5):833-49.
37. Beaulieu D, Fathi R, Srivastava D, Nijhawan RI. Current perspectives on Mohs micrographic surgery for melanoma. Clin Cosmet Investig Dermatol. 2018;11:309-20.

38. Narayanan K, Hadid OH, Barnes EA. Mohs micrographic surgery versus surgical excision for periocular basal cell carcinoma. The Cochrane database of systematic reviews. 2014;2014(12):CD007041.
39. Cumberland L, Dana A, Liegeois N. Mohs micrographic surgery for the management of nonmelanoma skin cancers. Facial Plast Surg Clin North Am. 2009;17(3):325-35.
40. Dahlstrand U, Sheikh R, Malmsjo M. Photoacoustic imaging for intraoperative micrographic control of the surgical margins of eyelid tumours. Acta Ophthalmol. 2020;98(2):e264-e5.
41. Ring C, Cox N, Lee JB. Dermatoscopy. Clin Dermatol. 2021;39(4):635-42.
42. Sinz C, Tschandl P, Rosendahl C, Akay BN, Argenziano G, Blum A, Braun RP, Cabo H, Gourhant JY, Kreusch J, Lallas A, Lapins J, Marghoob AA, Menzies SW, Paoli J, Rabinovitz HS, Rinner C, Scope A, Soyer HP, Thomas L, Zalaudek I, Kittler H. Accuracy of dermatoscopy for the diagnosis of nonpigmented cancers of the skin. Journal of the American Academy of Dermatology. 2017;77(6):1100-9.
43. Cerci FB, Kubo EM, Werner B, Tolkachjov SN. Dermoscopy accuracy for lateral margin assessment of distinct basal cell carcinoma subtypes treated by Mohs micrographic surgery in 368 cases. Int J Dermatol. 2022;61(4):e139-e41.
44. Gurgen J, Gatti M. Epiluminescence microscopy (dermoscopy) versus visual inspection during Mohs microscopic surgery of infiltrative basal cell carcinoma. Dermatol Surg. 2012;38(7 Pt 1):1066-9.
45. Mogensen M, Nurnberg BM, Forman JL, Thomsen JB, Thrane L, Jemec GB. In vivo thickness measurement of basal cell carcinoma and actinic keratosis with optical coherence tomography and 20-MHz ultrasound. Br J Dermatol. 2009;160(5):1026-33.
46. Cheng HM, Guitera P. Systematic review of optical coherence tomography usage in the diagnosis and management of basal cell carcinoma. Br J Dermatol. 2015;173(6):1371-80.
47. Jerjes W, Hamdoon Z, Al-Rawi N, Hopper C. Optical coherence tomography in the assessment of cutaneous cancer margins of the face: An immediate ex vivo study. Photodiagnosis Photodyn Ther. 2020;29:101616.
48. Pomerantz R, Zell D, McKenzie G, Siegel DM. Optical Coherence Tomography Used as a Modality to Delineate Basal Cell Carcinoma prior to Mohs Micrographic Surgery. Case Rep Dermatol. 2011;3(3):212-8.
49. Adan F, Kallen EJJ, Dermont G, Muche JM, Sinx KAE, Schilder A, Abdul Hamid M, Nelemans PJ, Mosterd K. Diagnostic accuracy of optical coherence tomography in the assessment of in vivo primary basal cell carcinoma resection margins prior to Mohs Micrographic Surgery. Journal of the European Academy of Dermatology and Venereology : JEADV. 2022;36(4):e270-e2.
50. Levine A, Markowitz O. Introduction to reflectance confocal microscopy and its use in clinical practice. JAAD Case Rep. 2018;4(10):1014-23.
51. Larson B, Abeytunge S, Seltzer E, Rajadhyaksha M, Nehal K. Detection of skin cancer margins in Mohs excisions with high-speed strip mosaicing confocal microscopy: a feasibility study. Br J Dermatol. 2013;169(4):922-6.

52. Guitera P, Menzies SW, Longo C, Cesinaro AM, Scolyer RA, Pellacani G. In vivo confocal microscopy for diagnosis of melanoma and basal cell carcinoma using a two-step method: analysis of 710 consecutive clinically equivocal cases. J Invest Dermatol. 2012;132(10):2386-94.
53. Xiong YD, Ma S, Li X, Zhong X, Duan C, Chen Q. A meta-analysis of reflectance confocal microscopy for the diagnosis of malignant skin tumours. Journal of the European Academy of Dermatology and Venereology : JEADV. 2016;30(8):1295-302.
54. Xiong YQ, Ma SJ, Mo Y, Huo ST, Wen YQ, Chen Q. Comparison of dermoscopy and reflectance confocal microscopy for the diagnosis of malignant skin tumours: a meta-analysis. J Cancer Res Clin Oncol. 2017;143(9):1627-35.
55. Venturini M, Gualdi G, Zanca A, Lorenzi L, Pellacani G, Calzavara-Pinton PG. A new approach for presurgical margin assessment by reflectance confocal microscopy of basal cell carcinoma. Br J Dermatol. 2016;174(2):380-5.
56. Guitera P, Moloney FJ, Menzies SW, Stretch JR, Quinn MJ, Hong A, Fogarty G, Scolyer RA. Improving management and patient care in lentigo maligna by mapping with in vivo confocal microscopy. JAMA Dermatol. 2013;149(6):692-8.
57. Menge TD, Hibler BP, Cordova MA, Nehal KS, Rossi AM. Concordance of handheld reflectance confocal microscopy (RCM) with histopathology in the diagnosis of lentigo maligna (LM): A prospective study. J Am Acad Dermatol. 2016;74(6):1114-20.
58. Pellacani G, De Carvalho N, Ciardo S, Ferrari B, Cesinaro AM, Farnetani F, Bassoli S, Guitera P, Star P, Rawson R, Rossi E, Magnoni C, Gualdi G, Longo C, Scope A. The smart approach: feasibility of lentigo maligna superficial margin assessment with hand-held reflectance confocal microscopy technology. Journal of the European Academy of Dermatology and Venereology : JEADV. 2018;32(10):1687-94.
59. Rajadhyaksha M, Gonzalez S, Zavislan JM. Detectability of contrast agents for confocal reflectance imaging of skin and microcirculation. J Biomed Opt. 2004;9(2):323-31.
60. Rajadhyaksha M, Marghoob A, Rossi A, Halpern AC, Nehal KS. Reflectance confocal microscopy of skin in vivo: From bench to bedside. Lasers in surgery and medicine. 2017;49(1):7-19.
61. Witkowski AM, Łudzik J, Arginelli F, Bassoli S, Benati E, Casari A, De Carvalho N, De Pace B, Farnetani F, Losi A, Manfredini M, Reggiani C, Malvehy J, Pellacani G. Improving diagnostic sensitivity of combined dermoscopy and reflectance confocal microscopy imaging through double reader concordance evaluation in telemedicine settings: A retrospective study of 1000 equivocal cases. PloS one. 2017;12(11):e0187748-e.
62. Hashemi P, Pulitzer MP, Scope A, Kovalyshyn I, Halpern AC, Marghoob AA. Langerhans cells and melanocytes share similar morphologic features under in vivo reflectance confocal microscopy: a challenge for melanoma diagnosis. Journal of the American Academy of Dermatology. 2012;66(3):452-62.
63. Levy J, Barrett DL, Harris N, Jeong JJ, Yang X, Chen SC. High-frequency ultrasound in clinical dermatology: a review. Ultrasound J. 2021;13(1):24.

64. Popescu DP, Choo-Smith LP, Flueraru C, Mao Y, Chang S, Disano J, Sherif S, Sowa MG. Optical coherence tomography: fundamental principles, instrumental designs and biomedical applications. Biophys Rev. 2011;3(3):155.
65. Sheng M, Tang M, Lin W, Guo L, He W, Chen W, Li K, Liu J, Xiao C, Li Y. The value of preoperative high-resolution MRI with microscopy coil for facial nonmelanoma skin cancers. Skin Res Technol. 2021;27(1):62-9.
66. Kang Y, Choi JA, Chung JH, Hong SH, Kang HS. Accuracy of preoperative MRI with microscopy coil in evaluation of primary tumor thickness of malignant melanoma of the skin with histopathologic correlation. Korean J Radiol. 2013;14(2):287-93.
67. Yao DK, Chen R, Maslov K, Zhou Q, Wang LV. Optimal ultraviolet wavelength for in vivo photoacoustic imaging of cell nuclei. J Biomed Opt. 2012;17(5):056004.
68. De la Zerda A, Zavaleta C, Keren S, Vaithilingam S, Bodapati S, Liu Z, Levi J, Smith BR, Ma TJ, Oralkan O, Cheng Z, Chen X, Dai H, Khuri-Yakub BT, Gambhir SS. Carbon nanotubes as photoacoustic molecular imaging agents in living mice. Nat Nanotechnol. 2008;3(9):557-62.
69. Jacques SL. Optical properties of biological tissues: a review. Phys Med Biol. 2013;58(11):R37-61.
70. Bell AG. The Production of Sound by Radiant Energy. Science. 1881;2(49):242-53.
71. Rosencwaig A. Photoacoustics and photoacoustic spectroscopy. New York: Wiley; 1980.
72. Das D, Sharma A, Rajendran P, Pramanik M. Another decade of photoacoustic imaging. Phys Med Biol. 2021;66(5).
73. Heijblom M, Piras D, van den Engh FM, van der Schaaf M, Klaase JM, Steenbergen W, Manohar S. The state of the art in breast imaging using the Twente Photoacoustic Mammoscope: results from 31 measurements on malignancies. Eur Radiol. 2016;26(11):3874-87.
74. Lin L, Hu P, Shi J, Appleton CM, Maslov K, Li L, Zhang R, Wang LV. Single-breath-hold photoacoustic computed tomography of the breast. Nat Commun. 2018;9(1):2352.
75. Wang Y, Zhan Y, Tiao M, Xia J. Review of methods to improve the performance of linear array-based photoacoustic tomography. Journal of Innovative Optical Health Sciences. 2019;13(02):2030003.
76. Xia J, Yao J, Wang LV. Photoacoustic tomography: principles and advances. Electromagn Waves (Camb). 2014;147:1-22.
77. Dean-Ben XL, Razansky D, Ntziachristos V. The effects of acoustic attenuation in optoacoustic signals. Phys Med Biol. 2011;56(18):6129-48.
78. Taruttis A, Ntziachristos V. Advances in real-time multispectral optoacoustic imaging and its applications. Nature photonics. 2015;9(4):219-27.
79. Attia ABE, Balasundaram G, Moothanchery M, Dinish US, Bi R, Ntziachristos V, Olivo M. A review of clinical photoacoustic imaging: Current and future trends. Photoacoustics. 2019;16:100144.

80. Mallidi S, Luke GP, Emelianov S. Photoacoustic imaging in cancer detection, diagnosis, and treatment guidance. Trends Biotechnol. 2011;29(5):213-21.
81. Kim G, Huang SW, Day KC, O'Donnell M, Agayan RR, Day MA, Kopelman R, Ashkenazi S. Indocyanine-green-embedded PEBBLEs as a contrast agent for photoacoustic imaging. J Biomed Opt. 2007;12(4):044020.
82. Kim C, Cho EC, Chen J, Song KH, Au L, Favazza C, Zhang Q, Cobley CM, Gao F, Xia Y, Wang LV. In vivo molecular photoacoustic tomography of melanomas targeted by bioconjugated gold nanocages. ACS Nano. 2010;4(8):4559-64.
83. Li PC, Wang CR, Shieh DB, Wei CW, Liao CK, Poe C, Jhan S, Ding AA, Wu YN. In vivo photoacoustic molecular imaging with simultaneous multiple selective targeting using antibody-conjugated gold nanorods. Opt Express. 2008;16(23):18605-15.
84. Song KH, Stein EW, Margenthaler JA, Wang LV. Noninvasive photoacoustic identification of sentinel lymph nodes containing methylene blue in vivo in a rat model. J Biomed Opt. 2008;13(5):054033.
85. Stoffels I, Morscher S, Helfrich I, Hillen U, Leyh J, Burton NC, Sardella TC, Claussen J, Poeppel TD, Bachmann HS, Roesch A, Griewank K, Schadendorf D, Gunzer M, Klode J. Metastatic status of sentinel lymph nodes in melanoma determined noninvasively with multispectral optoacoustic imaging. Sci Transl Med. 2015;7(317):317ra199.
86. Stoffels I, Jansen P, Petri M, Goerdt L, Brinker TJ, Griewank KG, Poeppel TD, Schadendorf D, Klode J. Assessment of Nonradioactive Multispectral Optoacoustic Tomographic Imaging With Conventional Lymphoscintigraphic Imaging for Sentinel Lymph Node Biopsy in Melanoma. JAMA Netw Open. 2019;2(8):e199020.
87. Tsang VTC, Li X, Wong TTW. A Review of Endogenous and Exogenous Contrast Agents Used in Photoacoustic Tomography with Different Sensing Configurations. Sensors (Basel, Switzerland). 2020;20(19).
88. Li D, Humayun L, Vienneau E, Vu T, Yao J. Seeing through the Skin: Photoacoustic Tomography of Skin Vasculature and Beyond. JID innovations : skin science from molecules to population health. 2021;1(3):100039.
89. Rebling J, Ben-Yehuda Greenwald M, Wietecha M, Werner S, Razansky D. Long-Term Imaging of Wound Angiogenesis with Large Scale Optoacoustic Microscopy. Adv Sci (Weinh). 2021;8(13):2004226.
90. Lin R, Chen J, Wang H, Yan M, Zheng W, Song L. Longitudinal label-free optical-resolution photoacoustic microscopy of tumor angiogenesis in vivo. Quant Imaging Med Surg. 2015;5(1):23-9.
91. Wang Y, Xu D, Yang S, Xing D. Toward in vivo biopsy of melanoma based on photoacoustic and ultrasound dual imaging with an integrated detector. Biomed Opt Express. 2016;7(2):279-86.
92. Yao J, Song L, Wang LV. Photoacoustic microscopy: superdepth, superresolution, and superb contrast. IEEE Pulse. 2015;6(3):34-7.
93. Oh JT, Li ML, Zhang HF, Maslov K, Stoica G, Wang LV. Three-dimensional imaging of skin melanoma in vivo by dual-wavelength photoacoustic microscopy. J Biomed Opt. 2006;11(3):34032.

94. Zhang HF, Maslov K, Stoica G, Wang LV. Functional photoacoustic microscopy for high-resolution and noninvasive in vivo imaging. Nat Biotechnol. 2006;24(7):848-51.
95. Kratkiewicz K, Manwar R, Rajabi-Estarabadi A, Fakhoury J, Meiliute J, Daveluy S, Mehregan D, Avanaki KM. Photoacoustic/Ultrasound/Optical Coherence Tomography Evaluation of Melanoma Lesion and Healthy Skin in a Swine Model. Sensors (Basel, Switzerland). 2019;19(12).
96. Varkentin A, Mazurenka M, Blumenrother E, Meinhardt-Wollweber M, Rahlves M, Broekaert SMC, Schad-Trcka S, Emmertinst S, Morgner U, Roth B. Comparative study of presurgical skin infiltration depth measurements of melanocytic lesions with OCT and high frequency ultrasound. J Biophotonics. 2017;10(6-7):854-61.
97. Breathnach A, Concannon E, Dorairaj JJ, Shaharan S, McGrath J, Jose J, Kelly JL, Leahy MJ. Preoperative measurement of cutaneous melanoma and nevi thickness with photoacoustic imaging. J Med Imaging (Bellingham). 2018;5(1):015004.
98. Favazza CP, Jassim O, Cornelius LA, Wang LV. In vivo photoacoustic microscopy of human cutaneous microvasculature and a nevus. J Biomed Opt. 2011;16(1):016015.
99. Schwarz M, Omar M, Buehler A, Aguirre J, Ntziachristos V. Implications of ultrasound frequency in optoacoustic mesoscopy of the skin. IEEE Trans Med Imaging. 2015;34(2):672-7.
100. Fredman G, Qiu Y, Ardigo M, Mogensen M. Skin tags imaged by reflectance confocal microscopy, optical coherence tomography and multispectral optoacoustic tomography at the bedside. Skin Res Technol. 2021;27(3):324-31.
101. Lavaud J, Coll JL, Cracowski JL, Blaise S, Josserand V. Photoacoustic imaging as an innovative technique for the exploration of blue rubber bleb naevus. Br J Dermatol. 2019;181(3):596-7.
102. Lin L, Zhang P, Xu S, Shi J, Li L, Yao J, Wang L, Zou J, Wang LV. Handheld optical-resolution photoacoustic microscopy. J Biomed Opt. 2017;22(4):41002.
103. Swearingen JA, Holan SH, Feldman MM, Viator JA. Photoacoustic discrimination of vascular and pigmented lesions using classical and Bayesian methods. J Biomed Opt. 2010;15(1):016019.
104. Chen Z, Rank E, Meiburger KM, Sinz C, Hodul A, Zhang E, Hoover E, Minneman M, Ensher J, Beard PC, Kittler H, Leitgeb RA, Drexler W, Liu M. Non-invasive multimodal optical coherence and photoacoustic tomography for human skin imaging. Sci Rep. 2017;7(1):17975.
105. Chuah SY, Attia AB, Long V, Ho CJ, Malempati P, Fu CY, Ford SJ, Lee JS, Tan WP, Razansky D, Olivo M, Thng S. Structural and functional 3D mapping of skin tumours with non-invasive multispectral optoacoustic tomography. Skin Res Technol. 2017;23(2):221-6.
106. Chuah SY, Attia ABE, Ho CJH, Li X, Lee JS, Tan MWP, Yong AA, Tan AWM, Razansky D, Olivo M, Thng STG. Volumetric Multispectral Optoacoustic Tomography for 3-Dimensional Reconstruction of Skin Tumors: A Further Evaluation with Histopathologic Correlation. J Invest Dermatol. 2019;139(2):481-5.

107. Attia ABE, Chuah SY, Razansky D, Ho CJH, Malempati P, Dinish US, Bi R, Fu CY, Ford SJ, Lee JS, Tan MWP, Olivo M, Thng STG. Noninvasive real-time characterization of non-melanoma skin cancers with handheld optoacoustic probes. Photoacoustics. 2017;7:20-6.
108. Zeitouni NC, Rohrbach DJ, Aksahin M, Sunar U. Preoperative Ultrasound and Photoacoustic Imaging of Nonmelanoma Skin Cancers. Dermatologic Surgery. 2015;41(4):525-8.
109. Ecclestone BR, Bell K, Abbasi S, Dinakaran D, Taher M, Mackey JR, Haji Reza P. Histopathology for Mohs micrographic surgery with photoacoustic remote sensing microscopy. Biomed Opt Express. 2021;12(1):654-65.
110. Dahlstrand U, Sheikh R, Merdasa A, Chakari R, Persson B, Cinthio M, Erlov T, Gesslein B, Malmsjo M. Photoacoustic imaging for three-dimensional visualization and delineation of basal cell carcinoma in patients. Photoacoustics. 2020;18:100187.
111. Park B, Bang CH, Lee C, Han JH, Choi W, Kim J, Park GS, Rhie JW, Lee JH, Kim C. 3D Wide-field Multispectral Photoacoustic Imaging of Human Melanomas In Vivo: A Pilot Study. Journal of the European Academy of Dermatology and Venereology : JEADV. 2020.
112. Zhou Y, Tripathi SV, Rosman I, Ma J, Hai P, Linette GP, Council ML, Fields RC, Wang LV, Cornelius LA. Noninvasive Determination of Melanoma Depth using a Handheld Photoacoustic Probe. J Invest Dermatol. 2017;137(6):1370-2.
113. Kim J, Kim YH, Park B, Seo HM, Bang CH, Park GS, Park YM, Rhie JW, Lee JH, Kim C. Multispectral ex vivo photoacoustic imaging of cutaneous melanoma for better selection of the excision margin. Br J Dermatol. 2018;179(3):780-2.
114. Ecclestone B, Dinakaran D, Haji Reza P. Single acquisition label-free histology-like imaging with dual-contrast photoacoustic remote sensing microscopy. J Biomed Opt. 2021;26(5).
115. Ruddell A, Croft A, Kelly-Spratt K, Furuya M, Kemp CJ. Tumors induce coordinate growth of artery, vein, and lymphatic vessel triads. BMC Cancer. 2014;14(1):354.
116. Langhout GC, Grootendorst DJ, Nieweg OE, Wouters MW, van der Hage JA, Jose J, van Boven H, Steenbergen W, Manohar S, Ruers TJ. Detection of melanoma metastases in resected human lymph nodes by noninvasive multispectral photoacoustic imaging. Int J Biomed Imaging. 2014;2014:163652.
117. Grootendorst DJ, Jose J, Wouters MW, van Boven H, Van der Hage J, Van Leeuwen TG, Steenbergen W, Manohar S, Ruers TJ. First experiences of photoacoustic imaging for detection of melanoma metastases in resected human lymph nodes. Lasers Surg Med. 2012;44(7):541-9.
118. Jose J, Grootendorst DJ, Vijn TW, Wouters MW, van Boven H, van Leeuwen TG, Steenbergen W, Ruers TJ, Manohar S. Initial results of imaging melanoma metastasis in resected human lymph nodes using photoacoustic computed tomography. J Biomed Opt. 2011;16(9):096021.
119. Ohta T, Shirakawa T, Okada S, Ishii N, Kiryu S. In vitro Demonstration of Melanoma Metastasis in Lymph Nodes of Prepared Specimens Using a Light-emitting Diode-based Multispectral Photoacoustic Ultrasound Imaging System. J Med Ultrasound. 2021;29(1):50-2.

120. Viator JA, Hazur M, Sajewski A, Tarhini A, Sanders ME, Edgar RH. Photoacoustic detection of circulating melanoma cells in late stage patients. J Innov Opt Health Sci. 2020;13(6).
121. Edgar RH, Tarhini A, Sander C, Sanders ME, Cook JL, Viator JA. Predicting Metastasis in Melanoma by Enumerating Circulating Tumor Cells Using Photoacoustic Flow Cytometry. Lasers Surg Med. 2021;53(4):578-86.
122. Hai P, Qu Y, Li Y, Zhu L, Shmuylovich L, Cornelius LA, Wang LV. Label-free high-throughput photoacoustic tomography of suspected circulating melanoma tumor cells in patients in vivo. J Biomed Opt. 2020;25(3):1-17.
123. Galanzha EI, Menyaev YA, Yadem AC, Sarimollaoglu M, Juratli MA, Nedosekin DA, Foster SR, Jamshidi-Parsian A, Siegel ER, Makhoul I, Hutchins LF, Suen JY, Zharov VP. In vivo liquid biopsy using Cytophone platform for photoacoustic detection of circulating tumor cells in patients with melanoma. Sci Transl Med. 2019;11(496).
124. Nedosekin DA, Sarimollaoglu M, Ye JH, Galanzha EI, Zharov VP. In vivo ultra-fast photoacoustic flow cytometry of circulating human melanoma cells using near-infrared high-pulse rate lasers. Cytometry A. 2011;79(10):825-33.
125. Johansen TH, Møllersen K, Ortega S, Fabelo H, Garcia A, Callico GM, Godtliebsen F. Recent advances in hyperspectral imaging for melanoma detection. WIREs Computational Statistics. 2019;12(1).
126. Lu G, Fei B. Medical hyperspectral imaging: a review. J Biomed Opt. 2014;19(1):10901.
127. Chin JA, Wang EC, Kibbe MR. Evaluation of hyperspectral technology for assessing the presence and severity of peripheral artery disease. J Vasc Surg. 2011;54(6):1679-88.
128. Greenman RL, Panasyuk S, Wang X, Lyons TE, Dinh T, Longoria L, Giurini JM, Freeman J, Khaodhiar L, Veves A. Early changes in the skin microcirculation and muscle metabolism of the diabetic foot. The Lancet. 2005;366(9498):1711-7.
129. Marotz J, Schulz T, Seider S, Cruz D, Aljowder A, Promny D, Daeschlein G, Wild T, Siemers F. 3D-perfusion analysis of burn wounds using hyperspectral imaging. Burns. 2021;47(1):157-70.
130. Ferris DG, Lawhead RA, Dickman ED, Holtzapple N, Miller JA, Grogan S, Bambot S, Agrawal A, Faupel ML. Multimodal hyperspectral imaging for the noninvasive diagnosis of cervical neoplasia. J Low Genit Tract Dis. 2001;5(2):65-72.
131. Panasyuk SV, Yang S, Faller DV, Ngo D, Lew RA, Freeman JE, Rogers AE. Medical hyperspectral imaging to facilitate residual tumor identification during surgery. Cancer Biol Ther. 2007;6(3):439-46.
132. Leon R, Martinez-Vega B, Fabelo H, Ortega S, Melian V, Castano I, Carretero G, Almeida P, Garcia A, Quevedo E, Hernandez JA, Clavo B, G MC. Non-Invasive Skin Cancer Diagnosis Using Hyperspectral Imaging for In-Situ Clinical Support. J Clin Med. 2020;9(6).

133. Christensen GB, Nagaoka T, Kiyohara Y, Johansson I, Ingvar C, Nakamura A, Sota T, Nielsen K. Clinical performance of a novel hyperspectral imaging device for cutaneous melanoma and pigmented skin lesions in Caucasian skin. Skin Res Technol. 2021;27(5):803-9.
134. Rasanen J, Salmivuori M, Polonen I, Gronroos M, Neittaanmaki N. Hyperspectral Imaging Reveals Spectral Differences and Can Distinguish Malignant Melanoma from Pigmented Basal Cell Carcinomas: A Pilot Study. Acta Derm Venereol. 2021;101(2):adv00405.
135. Nagaoka T, Kiyohara Y, Koga H, Nakamura A, Saida T, Sota T. Modification of a melanoma discrimination index derived from hyperspectral data: a clinical trial conducted in 2 centers between March 2011 and December 2013. Skin Res Technol. 2015;21(3):278-83.
136. Paoli J, Polonen I, Salmivuori M, Rasanen J, Zaar O, Polesie S, Koskenmies S, Pitkanen S, Overmark M, Isoherranen K, Juteau S, Ranki A, Gronroos M, Neittaanmaki N. Hyperspectral Imaging for Non-invasive Diagnostics of Melanocytic Lesions. Acta Derm Venereol. 2022;102:adv00815.
137. Neittaanmäki N, Salmivuori M, Pölönen I, Jeskanen L, Ranki A, Saksela O, Snellman E, Grönroos M. Hyperspectral imaging in detecting dermal invasion in lentigo maligna melanoma. British Journal of Dermatology. 2017;177(6):1742-4.
138. Neittaanmaki-Perttu N, Gronroos M, Jeskanen L, Polonen I, Ranki A, Saksela O, Snellman E. Delineating margins of lentigo maligna using a hyperspectral imaging system. Acta Derm Venereol. 2015;95(5):549-52.
139. Salmivuori M, Neittaanmaki N, Polonen I, Jeskanen L, Snellman E, Gronroos M. Hyperspectral imaging system in the delineation of Ill-defined basal cell carcinomas: a pilot study. Journal of the European Academy of Dermatology and Venereology : JEADV. 2019;33(1):71-8.
140. Neittaanmaki-Perttu N, Gronroos M, Tani T, Polonen I, Ranki A, Saksela O, Snellman E. Detecting field cancerization using a hyperspectral imaging system. Lasers Surg Med. 2013;45(7):410-7.
141. Tzoumas S, Ntziachristos V. Spectral unmixing techniques for optoacoustic imaging of tissue pathophysiology. Philos Trans A Math Phys Eng Sci. 2017;375(2107).
142. Tzoumas S, Deliolanis N, Morscher S, Ntziachristos V. Unmixing Molecular Agents From Absorbing Tissue in Multispectral Optoacoustic Tomography. IEEE Trans Med Imaging. 2014;33(1):48-60.
143. Tran KA, Kondrashova O, Bradley A, Williams ED, Pearson JV, Waddell N. Deep learning in cancer diagnosis, prognosis and treatment selection. Genome Med. 2021;13(1):152.
144. Ozturk S, Ozkaya U. Skin Lesion Segmentation with Improved Convolutional Neural Network. J Digit Imaging. 2020;33(4):958-70.
145. Mirikharaji Z, Abhishek K, Bissoto A, Barata C, Avila S, Valle E, Celebi ME, Hamarneh G. A survey on deep learning for skin lesion segmentation. Med Image Anal. 2023;88:102863.

146. Haggenmuller S, Maron RC, Hekler A, Utikal JS, Barata C, Barnhill RL, Beltraminelli H, Berking C, Betz-Stablein B, Blum A, Braun SA, Carr R, Combalia M, Fernandez-Figueras MT, Ferrara G, Fraitag S, French LE, Gellrich FF, Ghoreschi K, Goebeler M, Guitera P, Haenssle HA, Haferkamp S, Heinzerling L, Heppt MV, Hilke FJ, Hobelsberger S, Krahl D, Kutzner H, Lallas A, Liopyris K, Llamas-Velasco M, Malvehy J, Meier F, Muller CSL, Navarini AA, Navarrete-Dechent C, Perasole A, Poch G, Podlipnik S, Requena L, Rotemberg VM, Saggini A, Sangueza OP, Santonja C, Schadendorf D, Schilling B, Schlaak M, Schlager JG, Sergon M, Sondermann W, Soyer HP, Starz H, Stolz W, Vale E, Weyers W, Zink A, Krieghoff-Henning E, Kather JN, von Kalle C, Lipka DB, Frohling S, Hauschild A, Kittler H, Brinker TJ. Skin cancer classification via convolutional neural networks: systematic review of studies involving human experts. Eur J Cancer. 2021;156:202-16.

147. Tschandl P, Rosendahl C, Akay BN, Argenziano G, Blum A, Braun RP, Cabo H, Gourhant JY, Kreusch J, Lallas A, Lapins J, Marghoob A, Menzies S, Neuber NM, Paoli J, Rabinovitz HS, Rinner C, Scope A, Soyer HP, Sinz C, Thomas L, Zalaudek I, Kittler H. Expert-Level Diagnosis of Nonpigmented Skin Cancer by Combined Convolutional Neural Networks. JAMA Dermatol. 2019;155(1):58-65.

148. Anwar SM, Majid M, Qayyum A, Awais M, Alnowami M, Khan MK. Medical Image Analysis using Convolutional Neural Networks: A Review. J Med Syst. 2018;42(11):226.

149. Aloupogianni E, Ichimura T, Hamada M, Ishikawa M, Murakami T, Sasaki A, Nakamura K, Kobayashi N, Obi T. Hyperspectral imaging for tumor segmentation on pigmented skin lesions. J Biomed Opt. 2022;27(10).

150. La Salvia M, Torti E, Leon R, Fabelo H, Ortega S, Balea-Fernandez F, Martinez-Vega B, Castano I, Almeida P, Carretero G, Hernandez JA, Callico GM, Leporati F. Neural Networks-Based On-Site Dermatologic Diagnosis through Hyperspectral Epidermal Images. Sensors (Basel, Switzerland). 2022;22(19).

151. Schellenberg M, Dreher KK, Holzwarth N, Isensee F, Reinke A, Schreck N, Seitel A, Tizabi MD, Maier-Hein L, Grohl J. Semantic segmentation of multispectral photoacoustic images using deep learning. Photoacoustics. 2022;26:100341.

152. Ly CD, Nguyen VT, Vo TH, Mondal S, Park S, Choi J, Vu TTH, Kim CS, Oh J. Full-view in vivo skin and blood vessels profile segmentation in photoacoustic imaging based on deep learning. Photoacoustics. 2022;25:100310.

153. Khan U, Paheding S, Elkin CP, Devabhaktuni VK. Trends in Deep Learning for Medical Hyperspectral Image Analysis. IEEE Access. 2021;9:79534-48.

154. World Medical A. World Medical Association Declaration of Helsinki: ethical principles for medical research involving human subjects. JAMA. 2013;310(20):2191-4.

155. Sheikh R, Cinthio M, Dahlstrand U, Erlov T, Naumovska M, Hammar B, Zackrisson S, Jansson T, Reistad N, Malmsjo M. Clinical Translation of a Novel Photoacoustic Imaging System for Examining the Temporal Artery. IEEE Trans Ultrason Ferroelectr Freq Control. 2019;66(3):472-80.

156. Kass M, Witkin A, Terzopoulos D. Snakes: Active contour models. International Journal of Computer Vision. 1988;1(4):321-31.

157. Nielsen K, Zhao L, Stamnes J, Stamnes K, Moan J. The optics of human skin: Aspects important for human health2008.
158. Taruttis A, Claussen J, Razansky D, Ntziachristos V. Motion clustering for deblurring multispectral optoacoustic tomography images of the mouse heart. J Biomed Opt. 2012;17(1):016009.
159. Erlov T, Sheikh R, Dahlstrand U, Albinsson J, Malmsjo M, Cinthio M. Regional motion correction for in vivo photoacoustic imaging in humans using interleaved ultrasound images. Biomed Opt Express. 2021;12(6):3312-22.
160. Brozyna AA, Jozwicki W, Roszkowski K, Filipiak J, Slominski AT. Melanin content in melanoma metastases affects the outcome of radiotherapy. Oncotarget. 2016;7(14):17844-53.
161. Fehm TF, Deán-Ben XL, Ford SJ, Razansky D. In vivo whole-body optoacoustic scanner with real-time volumetric imaging capacity. Optica. 2016;3(11):1153-9.
162. Zhou Y, Li G, Zhu L, Li C, Cornelius LA, Wang LV. Handheld photoacoustic probe to detect both melanoma depth and volume at high speed in vivo. J Biophotonics. 2015;8(11-12):961-7.
163. Jeng GS, Li ML, Kim M, Yoon SJ, Pitre JJ, Jr., Li DS, Pelivanov I, O'Donnell M. Real-time interleaved spectroscopic photoacoustic and ultrasound (PAUS) scanning with simultaneous fluence compensation and motion correction. Nat Commun. 2021;12(1):716.
164. Zhou X, Akhlaghi N, Wear KA, Garra BS, Pfefer TJ, Vogt WC. Evaluation of Fluence Correction Algorithms in Multispectral Photoacoustic Imaging. Photoacoustics. 2020;19:100181.